

Developing Quantum Tunneling Contacts with Ultrathin AlN or ZrN on GaN

by

Kevin Jin-Huey Voon

A thesis submitted in partial fulfillment of the requirements for the degree of

Master of Science

in

Solid State Electronics

Department of Electrical and Computer Engineering  
University of Alberta

© Kevin Jin-Huey Voon, 2014

## Abstract

Gallium nitride (GaN) high-electron mobility transistors (HEMTs) have great potential for high-power and high-frequency applications, but current leakage issues compromise their reliability. This research focuses on developing GaN metal-oxide semiconductor field-effect transistors (MOSFETs), which produces higher current densities and breakdown voltages due to their natural off-state. Forming low-resistance ohmic contacts for the device can be accomplished by developing quantum tunneling contacts through an ultrathin AlN layer capable of generating high two-dimensional electron gas (2DEG) concentrations with GaN. This thesis will investigate the change in 2DEG and conductance with AlN thickness and GaN doping concentration, with AlN deposited using plasma-enhanced atomic layer deposition (PEALD) at 250°C. In addition, ZrN<sub>x</sub> is being considered as a possible alternative material for high electric field regions of the GaN MOSFET due to its greater breakdown capacity compared to AlN.

A peak 2DEG of  $2.2 \times 10^{13} \text{ cm}^{-2}$  was achieved with 4.5 nm of AlN on highly doped N<sup>+</sup> GaN ( $\sim 10^{18} \text{ cm}^{-3}$  concentration), measured through capacitance-voltage (C-V) profiling, with strain relaxation occurring at 6 nm. Although the 2DEG was theorized to not significantly change with doping concentration, the peak 2DEG was obtained at 6 nm at  $1.9 \times 10^{13} \text{ cm}^{-2}$  on unintentionally doped N<sup>-</sup> GaN ( $10^{14} \text{ cm}^{-3}$  concentration) while significantly lower values were reported for thinner layers. This suggests that higher doping leads to a greater degree of crystallinity with low-temperature ALD on GaN, as the lower 2DEG in N<sup>-</sup> GaN was attributed to acceptor-like interface traps. The conductance, derived from current-voltage (I-V) plots, was found to vary primarily due to 2DEG for N<sup>+</sup> GaN, and a contact resistance of  $< 0.5 \text{ } \Omega \cdot \text{mm}$  (contact resistivity of  $2 \times 10^{-4} \text{ } \Omega \cdot \text{cm}^2$ ) was achieved with 3 nm of AlN deposited. The N<sup>-</sup> GaN

conductance varied primarily by thickness, specifically, the transmission coefficient through AlN. An ohmic I-V curve was reported for 3 nm while higher thicknesses produced a non-ohmic relation. This characteristic was also observed after post-deposition annealing.

Initial measurements of semiconducting  $ZrN_x$  (with  $x=1.15$ ) indicated a closely matched work function and electron affinity with GaN and Al metal, since high 2DEG and ohmic contacts were only achieved with Al contacts on N+ GaN compared to Cr contacts or N- GaN. In addition, the 2DEG showed minimal variation with  $ZrN_x$  thickness, with any differences attributed to interface traps. Although as-deposited  $ZrN_x$  reported high  $2 \times 10^{-2} \Omega \cdot \text{cm}^2$  contact resistivity, post-deposition annealing at  $900^\circ\text{C}$  for 1 minute led to a tenfold decrease to  $2 \times 10^{-3} \Omega \cdot \text{cm}^2$  for 4 nm of  $ZrN_x$  on N+ GaN. With 1 nm of  $ZrN_x$ , the minimum contact resistivity was  $5 \times 10^{-3} \Omega \cdot \text{cm}^2$ , achieved at  $800^\circ\text{C}$  annealing. Future work will investigate the  $ZrN_x$  stoichiometry spectrum in order to lower the contact resistivity further.

## Preface

The work outlined in this thesis was a collaborative effort led by Dr. Douglas Barlage of the Electrical and Computer Engineering Department of the University of Alberta, with Dr. Ken Cadien of the Chemical and Materials Engineering Department as the lead collaborator. Kyle Bothe contributed the  $ZrN_x$  reliability tests and overarching MOSFET design described in Chapter 1, as well as the TLM plots outlined in Chapter 3. Pouyan Motamedi and Dr. Ken Cadien contributed the ALD process and XRD plot described in Chapter 2 and 3 respectively. Gem Shoute and Triratna Muneshwar participated in developing the  $ZrN_x$  experimental design in Chapters 4 and 5, with Muneshwar also performing the ALD and material characterization, including XPS. The rest is my original work.

Two publications have resulted from the AlN/GaN information presented in this thesis, particularly Chapter 3, with the above mentioned contributions also included. The first is a presentation at the 2014 CS MANTECH Conference in Denver, Colorado, USA, and the second is a publication in IOP Journal of Physics D. Both have been referenced in this work.

# Acknowledgements

First, I would like to thank my supervisor and friend Dr. Douglas Barlage for everything he's done to mold me into the researcher I am today. I greatly appreciate his optimism, his insight, and his keeping me in line whenever I got too agitated. I would also like to give a shout-out to my lab group for their support: Kyle Bothe, Alex Ma, Brett Carnio, Mourad Benlamri, and most of all, Lhing Gem Shoute for being a very dear friend. We learned a lot from each other about our research and about life. I would also like to thank our collaborator Dr. Ken Cadien and his lab group, with special thanks to Triratna Muneshwar for his dedication to the ZrN project.

I would like to thank the Department of Electrical and Computer Engineering for funding my research with the Queen Elizabeth II Graduate Student Scholarship. I also acknowledge Alberta Advanced Education's Achievement Scholarship program for providing further funding and recognizing my academic achievement.

Last, but not least, I would like to thank my parents for their financial and emotional support, for instilling in me the work ethic needed to be an effective researcher. Special thanks go out to my brother, Ryan Voon, for being an excellent roommate.

# Table of Contents

<b>Abstract.....</b>	<b>ii</b>
<b>Preface.....</b>	<b>iv</b>
<b>Acknowledgements.....</b>	<b>v</b>
<b>Table of Contents.....</b>	<b>vi</b>
<b>List of Figures.....</b>	<b>ix</b>
<b>List of Tables.....</b>	<b>x</b>
<b>List of Abbreviations.....</b>	<b>xi</b>
<b>1 Overview.....</b>	<b>1</b>
1.0 Motivation.....	1
1.1 Gallium nitride MOSFET.....	1
1.2 Band energy theory and polarization.....	5
1.3 Charge conservation and surface states.....	7
1.4 AlN/GaN polarization.....	8
1.5 ZrN <sub>x</sub> as an alternative material.....	10
<b>2 Fabrication and Characterization.....</b>	<b>12</b>
2.1 Plasma-enhanced atomic layer deposition.....	12
2.2 X-ray diffraction.....	14
2.3 Fabrication process.....	15
2.4 MOSCAP and C-V profiling method.....	20
2.5 TLM and I-V profiling method.....	24

<b>3</b>	<b>AlN/GaN.....</b>	<b>26</b>
3.1	Overview.....	26
3.2	Crystallinity analysis.....	27
3.3	C-V analysis.....	28
3.4	Band structure and 2DEG.....	30
3.5	Quantum tunneling and I-V analysis.....	37
3.6	Effects of annealing on N- GaN.....	43
<b>4</b>	<b>Semiconducting ZrN<sub>x</sub>/GaN.....</b>	<b>45</b>
4.1	Overview.....	45
4.2	Band structure predictions.....	46
4.3	Elemental composition of ZrN <sub>x</sub> .....	49
4.4	C-V and 2DEG analysis.....	50
4.5	I-V and contact analysis.....	52
4.6	Effect of annealing on contact resistance.....	54
<b>5</b>	<b>Conclusion.....</b>	<b>58</b>
5.1	Process summary.....	58
5.2	Key observations.....	59
5.3	Future work.....	60
5.4	Final remarks.....	63
<b>6</b>	<b>References.....</b>	<b>64</b>

## List of Figures

1-1 Schematic comparison of GaN HEMT and GaN MOSFET.....	3
1-2 Energy band diagrams comparing Schottky contact and quantum tunneling contact.....	4
1-3 AlN/GaN space charge components.....	7
1-4 Lifetime assessment of ZrN <sub>x</sub> /GaN heterojunction.....	11
2-1 ALD cycle schematic.....	12
2-2 Ellipsometry plot of thickness compared to number of ALD cycles.....	14
2-3 Metal etch patterning process flow.....	18
2-4 Lift-off deposition process flow.....	19
2-5 Planar MOSCAP and equivalent circuit model.....	20
2-6 1/C <sup>2</sup> -V plot of AlN on N- GaN.....	23
2-7 TLM structure and plot indicating contact and sheet resistance.....	24
3-1 XRD plot for 20 μm AlN on Si(111) at 250°C deposition.....	27
3-2 C-V plots of 3-6 nm AlN on N+ and N- GaN.....	28
3-3 C-F plot of 55 cycles of AlN on N+ GaN.....	28
3-4 Band diagrams for AlN/GaN.....	30
3-5 Plot of simulated and measured 2DEG for AlN/GaN.....	32
3-6 C-F plots for AlN on N- GaN.....	34
3-7 C-V plots of AlN on N- GaN with highlighted threshold voltages.....	35
3-8 Plot of transmission coefficient against AlN thickness.....	37
3-9 I-V plots of 3-6 nm AlN on N+ and N- GaN.....	39
3-10 I-V plots with varied measurement temperatures for AlN/GaN.....	39
3-11 Plot of conductance against 2DEG concentration for AlN/GaN.....	40
3-12 TLM-derived resistance and mobility for 40 cycles of AlN on N+ GaN.....	41
4-1 Simulated AlGaIn/GaN HEMT electric field distribution.....	45
4-2 Band diagrams for ZrN <sub>x</sub> /GaN.....	47
4-3 XPS plot of ZrN <sub>x</sub> /GaN.....	49
4-4 C-V plots and 2DEG concentration for 1-7 nm of ZrN on N+ GaN .....	51
4-5 I-V plots of ZrN/GaN.....	53
4-6 I-V plots of 4 nm of ZrN on N+ GaN after annealing from 700-900°C.....	55

4-7 Plot of contact resistance against annealing temperature for ZrN/GaN.....	56
5-1 I-V family of curves for N- GaN MOSFET with 40 cycles of AlN.....	61
5-2 I-V plots of 40 cycles of AlN on N- GaN after annealing from 400-900°C.....	62

## List of Tables

1-1 Physical properties of prominent semiconductors.....	2
1-2 Figures of merit for prominent semiconductors.....	2
1-3 Polarization constants for various wurtzite materials.....	9
3-1 Simulation parameters of the AlN/GaN heterojunction.....	30
3-2 Summary of MOSCAP CV and transmission coefficient results for AlN/GaN.....	32
3-3 Comparison of AlN trap charge and threshold voltage with thickness on N- GaN.....	35
3-4 TLM-derived resistance and effective mobility for 40 cycles of AlN on N+ GaN.....	41
3-5 Variation of conductance with annealing temperature for 40 cycles of AlN on N- GaN.....	43
4-1 Comparison of simulated transmission coefficients for ZrN <sub>x</sub> /GaN.....	47
4-2 Simulation parameters for the ZrN <sub>x</sub> /GaN heterojunction.....	48
4-3 Elemental composition of ZrN <sub>x</sub> .....	50
4-4 Comparison of 2DEG and interface trap concentrations with varying ZrN thickness.....	52
4-5 Comparison of TLM-derived resistances at varying annealing temperatures.....	56

## List of Abbreviations

GaN – Gallium Nitride

AlN – Aluminum Nitride

ZrN<sub>x</sub> – Zirconium Nitride

ZrO<sub>2</sub> – Zirconium Oxide

FET – Field-Effect Transistor

HEMT – High Electron Mobility Transistor

MOSFET – Metal Oxide Semiconductor Field Effect Transistor

2DEG – Two-Dimensional Electron Gas

ALD – Atomic Layer Deposition

PEALD – Plasma-Enhanced Atomic Layer Deposition

MBE – Molecular-Beam Epitaxy

C-V – Capacitance-Voltage

C-F – Capacitance-Frequency

G<sub>p</sub>/ω-F – Conductance-Frequency (normalized)

D<sub>it</sub> – Density of Interface States

I-V – Current Voltage

XRD – X-Ray Diffraction

XPS – X-ray Photoelectron Spectroscopy

MOSCAP – Metal Oxide Semiconductor Capacitor

TLM – Transfer Length Model

# Chapter 1: Overview

## 1.0 Summary

This work outlines the use of low-temperature atomic layer deposition to produce AlN/GaN and ZrN<sub>x</sub>/GaN heterojunctions for low-resistance ohmic contacts in GaN MOSFETs.

Chapter 1 outlines the theory and motivation for investigating these material systems.

Chapter 2 explains in greater detail the ALD process and the fabrication and characterization of the MOSCAP device and transfer length method (TLM) structures.

Chapters 3 and 4 display and analyze the material and electrical results of the AlN and ZrN<sub>x</sub> barriers respectively.

Chapter 5 summarizes the previous chapters and outlines implications for future research.

## 1.1 Gallium nitride MOSFET

Gallium nitride (GaN), as a wide band gap ( $E_g = 3.4$  eV) material, has great potential for producing transistors with high power and low switching losses. It enables a high critical breakdown electric field ( $E_c = 3.3$  MV/cm, Table 1-1) [1] and operating temperatures higher than 200°C. GaN is widely pursued for devices handling high-voltage power transfer and conversion while greatly reducing conduction and switching power losses. The former, specifically, the on-resistance of the drift region in a semiconductor device, can be assessed by Baliga's figure of merit (BFM) [2], which is given by the formula:

$$BFM = \epsilon * \mu * E_c^3 \quad (1.1)$$

	Si	GaAs	4H-SiC	6H-SiC	GaN	Diamond
$E_g$ (eV)	1.1	1.4	3.26	3.0	<b>3.39</b>	5.45
$\epsilon_r$	11.8	12.8	10	9.7	<b>9</b>	5.5
$\mu_n$ (cm <sup>2</sup> /Vs)	1350	8500	370 <sup>a</sup> 650 <sup>b</sup>	370 <sup>a</sup> 50 <sup>b</sup>	<b>900</b>	1900
$E_c$ (MV/cm)	0.3	0.4	2.0	2.4	<b>3.3</b>	5.6
$v_{sat}$ (10 <sup>7</sup> cm/s)	1.0	2.0	2.0	2.0	<b>2.5</b>	2.7
$\lambda$ (W/cm s)	1.5	0.5	4.5	4.5	<b>1.3</b>	20

<sup>a</sup> Mobility along a-axis

<sup>b</sup> Mobility along c-axis

**Table 1-1:** Physical properties of prominent semiconductors in power electronic devices [1]. The variables  $v_{sat}$  and  $\lambda$  refer to electron saturation velocity and thermal conductivity respectively.

Figure of Merit	Formula	Si	GaAs	4H-SiC	6H-SiC	GaN	Diamond
BFM	$\epsilon\mu E_c^3$	1	15.6	130	110	<b>650</b>	4110
BHFFM	$\mu E_c^2$	1	10.8	22.9	16.8	<b>77.8</b>	470
JFM	$(E_c v_{sat}/\pi)^2$	1	7.1	180	260	<b>760</b>	2540
KFM	$\lambda(v_{sat}/\epsilon)^{1/2}$	1	0.45	4.61	4.68	<b>1.6</b>	32.1

**Table 1-2:** Figures of merit for prominent semiconductors [1] derived from Table 1-1. The abbreviations, in order, refer to Baliga's figure of merit, Baliga's high frequency figure of merit, Johnson's figure of merit, and Keyes' Figure of Merit for thermal limitations to power switching.

Here,  $\epsilon$  is the electrical permittivity of the material (a product of the relative permittivity  $\epsilon_r$ , also referred to as the dielectric constant  $\kappa$  in some instances, and the free space permittivity  $\epsilon_0=8.854 \times 10^{-14}$  F/cm) and  $\mu$  is the charge carrier mobility. This formula claims an on-resistance improvement of 650 times over silicon [1] at the same breakdown field (Table 1-2). It also claims a 760 Johnson's figure of merit (JFM) for high-frequency capability relative to silicon. These advantages have made it a prime candidate for high-electron mobility transistors (HEMTs) operating at high frequencies, which are currently in production by major companies including TriQuint<sup>1</sup> and Toshiba<sup>2</sup>. Their design is centred on generating the two-dimensional electron gas

<sup>1</sup> <http://www.triquint.com/applications/defense/gan-products>

<sup>2</sup> <http://www.toshiba.com/taec/Catalog/Line.do?familyid=18&lineid=900254>

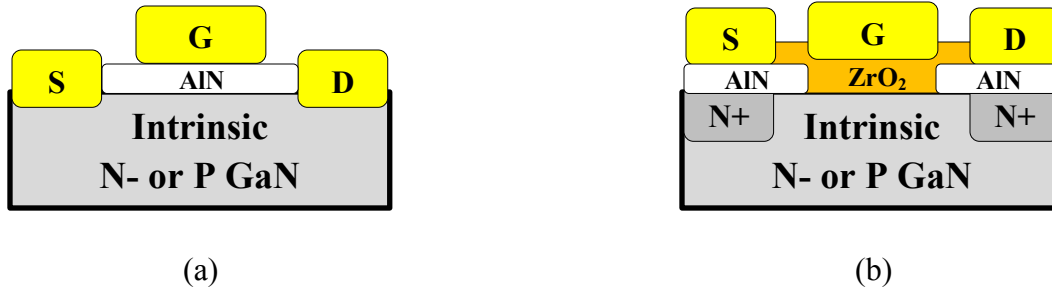


**Figure 1-1:** Schematic comparison of (left) GaN HEMT and (right) GaN MOSFET.

(2DEG) first discovered in aluminum gallium nitride (AlGaN) on GaN in 1992 [3].

Although HEMTs offer high mobility and on-resistance performance [4,5], their efficiency is limited by the structure's lack of an ideal off-state. The polarization-induced 2DEG charge generated by the AlGaN/GaN heterojunction is continuously present in the conduction channel since AlGaN covers the entire area between the source and drain (Fig. 1-1). The metal-oxide semiconductor field effect transistor (MOSFET), which uses variations in donor or acceptor electron impurities within the GaN substrate to form the channel, is by default in an off-state since the gate is separated from the channel by an insulating dielectric layer. In addition, the AlN layer is isolated from the conduction channel and the 2DEG is generated instead at the source/drain contacts. This structure provides greater efficiency and reliability compared to the HEMT due to its lower minimum carrier concentration [4], which leads to lowered avalanche breakdown. Simulations of the structure [5] compared to a state-of-the-art HEMT device [6] have demonstrated more than 2.5 times higher breakdown voltage and lower current leakage even with the gate length reduced from 8  $\mu\text{m}$  to 6  $\mu\text{m}$ . The ability to scale down the device enables the production of higher-speed devices while maintaining reliable switching performance. Because of these advantages, producing the GaN MOSFET is the project goal.

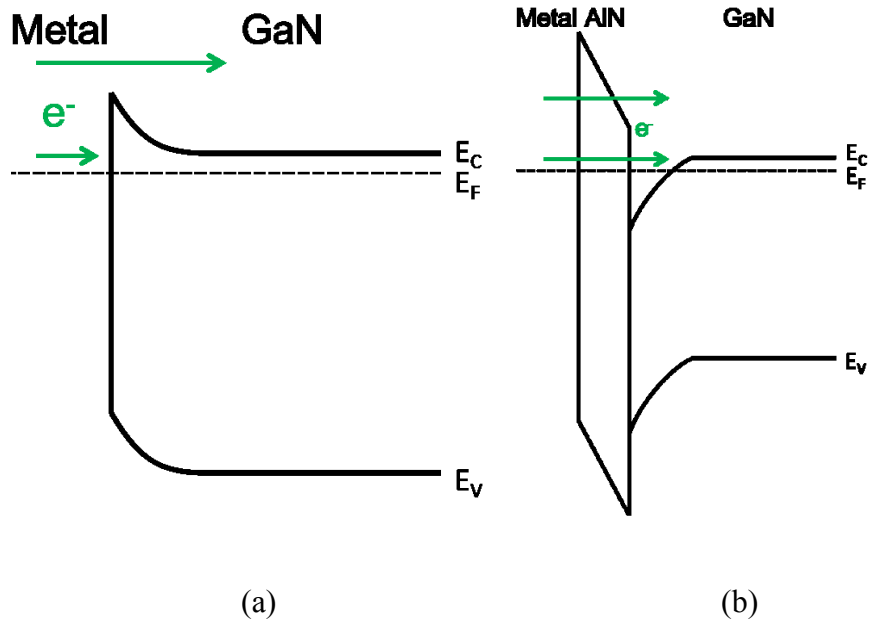


**Figure 1-2:** Energy band diagram representing electron ( $e^-$ ) transmission through (a) Schottky contact between metal and GaN and (b) quantum tunneling contact with an added ultrathin AlN barrier on GaN.  $E_C$ ,  $E_F$ , and  $E_V$  represent the conduction band, Fermi level, and valence band respectively.

Several challenges present themselves in developing a GaN MOSFET. A previously major issue was depositing a suitable gate oxide layer on GaN, since it is unable to form a native oxide. Its crystal lattice structure is mismatched with most oxides, leading to substantial defects and parasitic capacitance [7]. This problem was recently solved using the high- $\kappa$  dielectric zirconium oxide ( $ZrO_2$ ), which demonstrated a high  $>3.5 \mu F/cm^2$  capacitance density and  $375 \text{ cm}^2/Vs$  mobility [8]. Atomic layer deposition (ALD) was used to deposit the oxide, resulting in a uniform, conformal interface with minimum defects.

With the gate oxide layer established, producing low-resistance ohmic contacts (referring to a linear current-voltage relation) on GaN presents another problem for designing the MOSFET. Its high band gap presents a challenge in forming metal-GaN contacts, since most metals will form a Schottky energy barrier (Fig. 1-2a) which impedes electron transmission due

to their higher work function. Adding an ultrathin polarization barrier layer between the metal and GaN (Fig. 1-2b) creates an alternate transmission path for the electrons through quantum tunneling. Thus, generating a high 2DEG concentration at the interface provides a steady electron supply to promote continuous current flow through the barrier. Investigating aluminum nitride (AlN), which theoretically maximizes the 2DEG generated by the AlGaN/GaN heterojunction, and zirconium nitride (ZrN), which offers material stability, for use in these tunneling contacts will be the focus of this research.

A third issue with developing a GaN MOSFET involves introducing impurities, or dopants. The material is naturally n-type, with a larger electron concentration than hole concentration, and it can be easily doped to have a higher electron donor concentration, or N+ type. Doping GaN to have a greater hole concentration, making it p-type, is more difficult to achieve since the most currently available dopant, magnesium (Mg), tends to cause defects in the doping process. To circumvent this, undoped GaN (N-) is used as the main substrate material, forming a pseudo-junction. Though the built-in voltage would be significantly lower, the difference can be amplified with the 2DEG generated by the AlN/GaN contact junctions.

## 1.2 Band energy theory and polarization

Power electronic switching devices such as HEMTs generate electric charge based on a heterojunction of two different materials: a semiconductor base coated with a thin insulator film. Due to their differing band gaps, an energy discrepancy exists within their respective band structures. The Schottky barrier height between a metal and semiconductor or insulator,  $\Phi_b$  is given by:

$$\Phi_b = \Phi_m - \chi_s \quad (1.2)$$

where  $\Phi_m$  refers to the work function, the energy required to excite an electron to vacuum, and  $\chi_s$  is the semiconductor or insulator electron affinity. Similarly, the conduction band offset,  $\Delta E_c$ , is the difference in  $\chi_s$  between two semiconducting or insulating materials in a heterojunction.

The crystal lattice mismatch between the semiconductor and thin film leads to tensile strain between the materials. This creates a polarization-induced electric field which causes band bending in the thin film layer. The conduction band of the semiconducting layer consequently bends towards the interface to maintain vacuum energy continuity with the conduction band offset of the thin film layer, leading to the formation of a triangular quantum well at the interface. Since it falls below the Fermi level, it attracts and contains the 2DEG charge.

In a Schottky diode, the potential energy barrier is overcome through thermionic emission when the electrons gain energy higher than the potential barrier through an external source (Fig. 1-2a). This leads to an exponential current-voltage (I-V) characteristic since the electron transmission probability increases with voltage. Electron transport also depends on the Schottky barrier height, since the transmission probability increases exponentially with decreased barrier height. An ohmic contact usually results from  $\Phi_m$  being higher than  $\chi_s$ , in which case no barrier exists. However, these parameters are intrinsic to the materials and cannot be reliably modified. Instead, the contacts investigated in this research operate by quantum tunneling through the ultrathin AlN barrier to produce more consistent current flow (Fig. 1-2b), thus resulting in a linear, ohmic I-V characteristic. Since the electron transmission probability decreases exponentially with barrier thickness, high polarization with low AlN thickness and contact metal work function was the predicted goal for maximum tunneling current.

### 1.3 Charge conservation and surface states

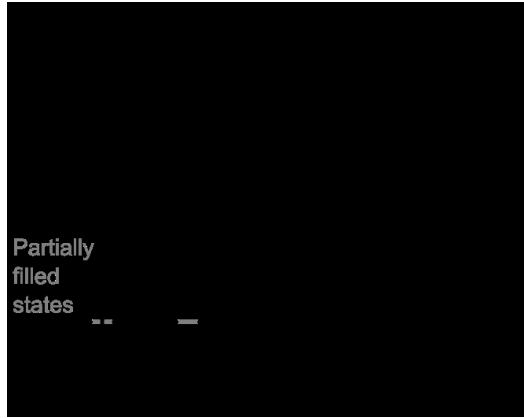


**Figure 1-3:** Band diagram [10] displaying the space charge components in the AlN/GaN heterojunction. Charge is transferred from the surface states to the 2DEG to maintain balance.

In an AlN barrier, charge conservation must be maintained among the various different space charge sources (Fig. 1-3 [9]). Assuming a buffer charge of 0, since its contribution is often negligible compared to the other sources, this is expressed in the formula:

$$Q_{Surface} + Q_{AlN} - Q_n = 0 \quad (1.3)$$

where  $Q_{Surface}$ ,  $Q_{AlN}$ , and  $Q_n$  represent the surface state charge, AlN doping charge, and 2DEG charge respectively.

For an undoped AlN barrier, where  $Q_{AlN}$  becomes 0 (as shown in Fig. 1-3):

$$Q_{Surface} = Q_n \quad (1.4)$$

This relation indicates that the number of electrons in the 2DEG is equal to the number of ionized donor-like surface states, which indicates that surface states are the source of the 2DEG [9]. The surface states are neutrally charged when filled with electrons, and positively charged when empty. Charge transfer occurs when the surface states gain enough energy to reach the

Fermi level, at which point electrons travel through the conduction band to empty, lower-energy states in the triangular quantum well at the GaN interface. When a surface state exists below the Fermi level, the state is filled and the overall charge is 0, resulting in no 2DEG. The surface states gain energy as a result of the polarization-induced electric field between AlN and GaN, which becomes stronger with increasing AlN thickness. Eventually, once AlN reaches a certain critical thickness, the donor-like states reach the Fermi level and the 2DEG starts to appear. The 2DEG has a logarithmic growth rate relative to the AlN thickness, with a high initial growth rate immediately past the critical thickness. As the barrier becomes thicker, the 2DEG charge and ionized surface states steadily weaken the polarization dipole and consequently, the polarization-induced electric field. Thus, the growth rate decreases until the 2DEG reaches an asymptotic limit, at which the AlN surface states become empty and no more charge can be transferred.

#### 1.4 AlN/GaN polarization

The III-V nitride (III-N) semiconductors each have a wurtzite crystal structure, a hexagonal prism with basal edge length  $a$  and height  $c$ . Polarization is measured in the (0001) direction, the direction of crystal growth, and consists of both a spontaneous component for each individual material at zero strain and piezoelectric polarization between the materials [10]. Spontaneous polarization constants  $P_{eq}$  for various materials are displayed in Table 1-3 [11], and the polarization constant for alloyed materials can be linearly interpolated from its original materials. For example, the polarization strength of  $Al_xGa_{1-x}N$ , where  $x$  is the percent concentration of Al, is expressed by the formula [10]:

$$P_{SP}(x) = (-0.052x - 0.029) C / m^2 \quad (1.5)$$

The piezoelectric polarization strain is calculated using Table 1-2 and the formula [10]:

	$P_{SP}$	$Z^*$	$du/d\varepsilon_3$	$e_{33}$	$e_{31}$	$e_{33}^{(0)}$	$e_{31}^{(0)}$
<b>AlN</b>	<b>-0.081</b>	<b>-2.70</b>	<b>-0.18</b>	<b>1.46</b>	<b>-0.60</b>	<b>-0.47</b>	<b>0.36</b>
<b>GaN</b>	<b>-0.029</b>	<b>-2.72</b>	<b>-0.16</b>	<b>0.73</b>	<b>-0.49</b>	<b>-0.84</b>	<b>0.45</b>
InN	-0.032	-3.02	-0.20	0.97	-0.57	-0.88	0.45
ZnO	-0.057	-2.11	-0.21	0.89	-0.51	-0.66	0.38
BeO	-0.045	-1.85	-0.06	0.02	-0.02	-0.60	0.35
ZnO	-0.05	-2.05	-0.25	1.21	-0.51	-0.58	0.37
BeO	-0.05	-1.72	-0.09	0.05		-0.29	

**Table 1-3:** Polarization constants in the c-axis direction for various wurtzite materials [11].  $P_{SP}$  refers to spontaneous polarization,  $Z^*$  is the axial component of the Born charge tensor,  $u$  is the anion-cation bond length,  $\varepsilon_j$  is the strain, and  $e_{ij}$  is the piezoelectric tensor. The subscripts  $i$  and  $j$  refer to the polarization direction, either 1 or 2 for in-plane or 3 for axial.

$$P_{PE}(x) = 2[r(x) - 1] \frac{a - a_0}{a_0} * (e_{31} - e_{33} \frac{C_{13}}{C_{33}}) \quad (1.6)$$

Here,  $a_0$  refers to the base material (e.g. GaN in AlGaN/GaN) while all other constants refer to the polarization material (e.g. AlGaN). The relaxation constant is represented by  $r(x)$ . Up until the strained layer reaches a certain thickness, which will be referred to as the strain relaxation onset, the junction experiences uniform strain. For polarization layers thicker than the relaxation onset, the piezoelectric polarization decreases linearly with  $r$  as a result of misfit crystal dislocations. As implied by the equation, the relaxation onset varies based on the material. As the Matthews-Blakeslee model [12,13] indicates, it occurs at thinner layers for higher values of  $x$ , reaching a minimum with non-alloyed ( $x=1$ ) polarization layer materials. Consequently, although pure AlN produces the highest polarization strain with GaN as Equations 1.5 and 1.6 indicate, the alloyed AlGaN is used for layers thicker than 5 nm.

Both AlGaN and GaN have particularly high spontaneous polarization and piezoelectric constants compared to typical III-V and II-VI semiconductors (Table 1-2), and aluminum nitride (AlN) in particular has the highest parameters among all the binary semiconductors. Thus, the

polarization between AlN and GaN potentially produces extremely high 2DEG concentrations, up to a theoretical limit of  $6.4 \times 10^{13} \text{ cm}^{-2}$  when fully strained [10]. However, this is not obtainable in practice since its high tensile strain, which results from the materials' crystal lattice mismatch of 2.4%, leads to relaxation at very thin layers of AlN [14,15]. Micro-cracks can be observed as early as 5 nm [16]. For this reason, the alloy AlGaIn has historically been used as the barrier layer for GaN HEMTs. Recent developments in AlN/GaN research have resulted from more advanced deposition methods to precisely deposit materials in the nanometre range. In addition, ultrathin AlN is conducive to quantum tunneling, which, along with the high 2DEG, is promising for developing GaN MOSFET contacts.

### **1.5 ZrN<sub>x</sub> as an alternative material**

Zirconium nitride is a material that varies from conducting to insulating depending on its nitrogen concentration (indicated as x in ZrN<sub>x</sub>), with ZrN being metallic and Zr<sub>3</sub>N<sub>4</sub> being insulating [17]. It is widely used in industrial applications as a protective coating due to its ability to withstand high wear, corrosion, and temperatures. Reliability testing has shown that this resiliency also applies to electrical breakdown, and since AlN is prone to degradation in high electric fields, ZrN<sub>x</sub> is worth investigating as a possible alternative heterojunction material with GaN. AlN/GaN contacts have demonstrated increased contact resistance after 5 hours of annealing at 600°C while ZrN<sub>x</sub>/GaN contacts remain stable even after exposure at the same temperature for 1000 hours [18]. Furthermore, our electrical stress characterization tests (Fig. 1-4) have shown that ZrN has an 8x lifetime improvement over AlN and can withstand 20 MV/cm breakdown fields compared to 2 MV/cm for AlN [19].

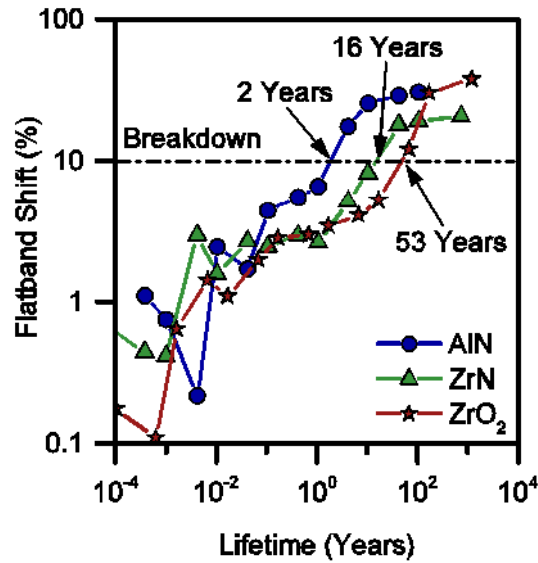


**Figure 1-4:** Lifetime assessment of the ZrN<sub>x</sub>/GaN heterojunction based on threshold voltage shifting during burn-in tests (courtesy of Kyle Bothe).

While AlN's high band gap and band offset deters thermionic emission, ZrN<sub>x</sub>, which has a band gap above 2 eV [20], is predicted to have a conduction band structure more closely matched to GaN. The lower band offset between the two materials is more conducive to current flow and ohmic contacts have been previously achieved with the ZrN/GaN metal-semiconductor junction [21]. Although the contacts demonstrated a high contact resistance, its high electric field breakdown capacity is promising as an alternative material to AlN for the high-field regions of the GaN MOSFET. As a relatively unexplored material for its electrical characteristics, determining the material system's band structure and interactions with GaN will be a focus of this research.

## Chapter 2: Fabrication and characterization

### 2.1 Plasma-enhanced atomic layer deposition

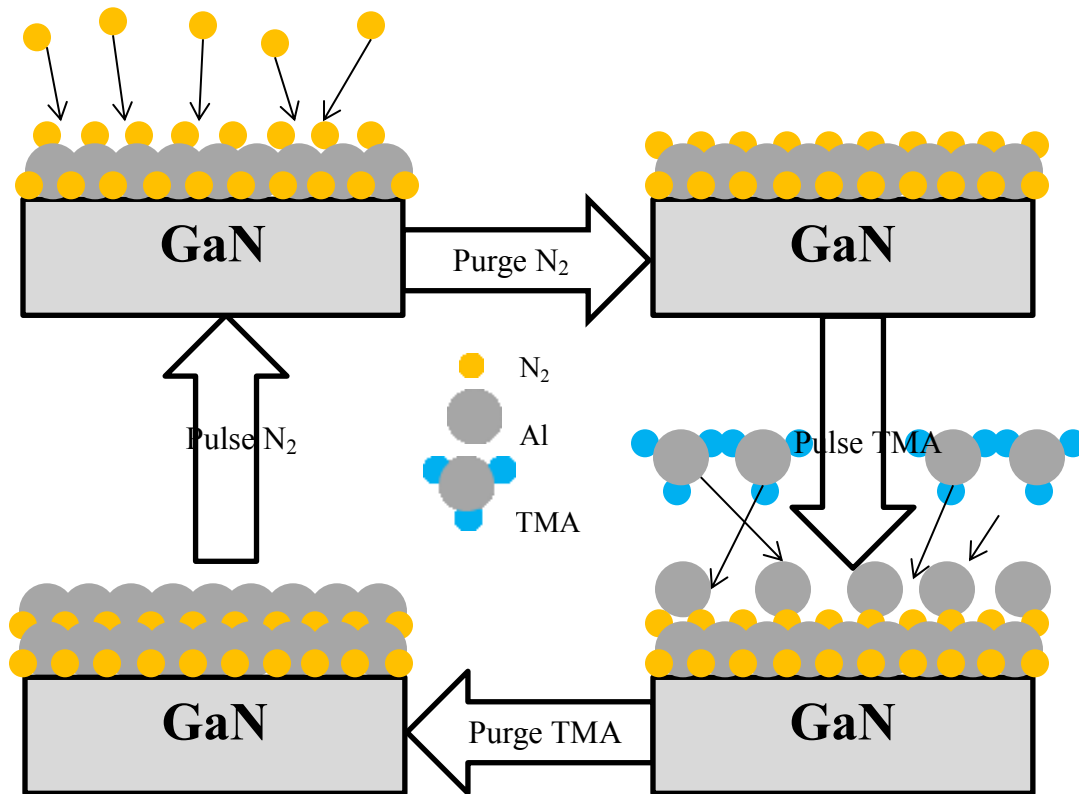


**Figure 2-1:** Schematic showing one ALD deposition cycle of filling and vacuum purging the chamber of each precursor.

Atomic layer deposition (ALD) is a process which deposits ultrathin material layers onto a surface through repeated cycles of self-limiting chemical reactions (Fig. 2-1). The two reaction chemicals, known as precursors, are alternately pulsed into the reaction chamber in specific quantities. After each precursor pulse, the deposition chamber is purged with a gas such as argon to prevent any undesired reactions. An ALD cycle thus consists of alternately releasing and purging each precursor, each reacting on the surface with the other to produce an atomic monolayer of the desired compound material. By repeating this process as many times as

required, this allows for precise thickness control at the angstrom scale while producing uniform and conformal thin films.

Our ALD system is capable of two deposition methods, thermal ALD and plasma-enhanced ALD (PEALD) [22]. With thermal ALD, energy is supplied by heating the substrate to a temperature typically within an ALD window of 200°C – 400°C. Plasma-enhanced atomic layer deposition (PEALD), which generates plasma of highly reactive ions and radicals from an RF energy source to supply the necessary reaction energy, is an alternative method that allows for lower process temperatures, as low as 25°C – 100°C depending on the material [23]. This allows deposition to be performed on substrates with heat-sensitive materials such as polymers and the photoresist used for lift-off processes. The latter is particularly beneficial for developing GaN MOSFET devices. Since virtually all available AlN chemical etchants also etch GaN at a faster rate [24], lift-off is better suited to selectively depositing and patterning ultrathin AlN.

The PEALD process was used to deposit the polarization layers on GaN at 250°C. Two GaN doping variations were tested; one highly doped (N<sup>+</sup>, found to be  $7 \times 10^{17} \text{ cm}^{-3}$  as explained in Section 2.4) and one left undoped (N<sup>-</sup>,  $\sim 10^{14} \text{ cm}^{-3}$  concentration). For AlN, trimethylaluminum (TMA) and nitrogen plasma precursors were employed. The exact layer thicknesses were determined from spectroscopic ellipsometry, which measured the changes in light polarization with its reflection in the thin film [22]. The measurements resulted in a highly linear plot of thickness with respect to the number of deposition cycles, from which the slope would indicate the deposition rate. AlN showed a 0.81 Å AlN deposition rate as shown in Fig. 2-2, while the ZrN<sub>x</sub> samples had a 1 Å deposition rate.

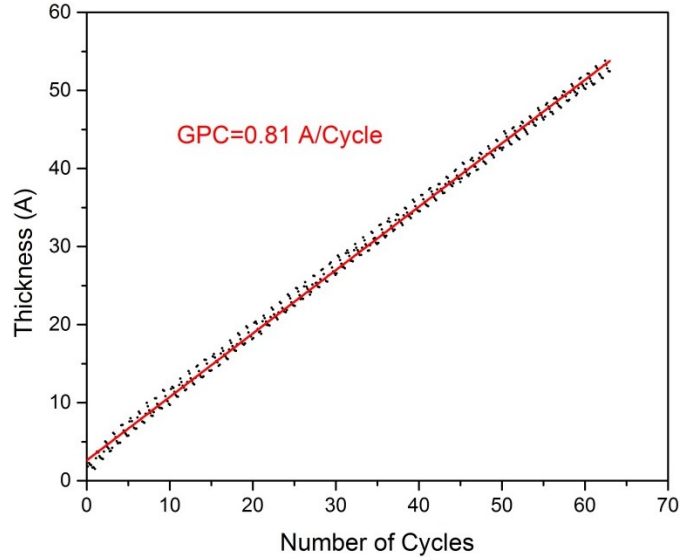


**Figure 2-2:** Relation between AlN thickness and number of ALD cycles on GaN.

## 2.2 X-ray diffraction

X-ray diffraction (XRD) is used to identify the crystal structure of the materials used in ALD, which can be used to predict their polarization behaviour. The crystal lattice, which is composed of uniformly spaced atoms based on their Miller index (hkl) direction, is treated as a diffraction grating for the incident x-rays of specified wavelength  $\lambda$ . At certain incident angles, the waves reflecting off the atoms will constructively interfere, creating intensity peaks in the XRD plot that can be interpreted according to Bragg's Law:

$$2d \sin \theta = n\lambda \quad (2.1)$$

The atomic spacing distance  $d$  is derived from the equation and compared to known specifically oriented crystal lattice constants. Here,  $n$  is an integer depending on the Miller index number. As previously stated, polarization in III-V nitride crystals occur in the direction perpendicular to the interface, or (002), due to their wurtzite structure. High XRD intensities in that direction would indicate a highly strained layer. In contrast, a higher (100) intensity

corresponding to the direction parallel to the interface would indicate significant strain relaxation. XRD measurements were performed on a sample with 20 nm of AlN on Si(111) to investigate the strength of polarization strain within the AlN layer, with the results detailed in Section 3.2. This is much thicker than the <6 nm used for AlN/GaN characterization, but the ultrathin layers required for tunneling contacts are impractical for XRD characterization due to the difficulty in achieving diffraction.

It should be noted that XRD analysis is difficult to perform on ultrathin films, and thus thicker layers are used to allow x-ray penetration. However, thin films have different crystal properties compared to thicker films, especially since AlN experiences strain relaxation at even relatively low thicknesses. Thus, this plot does not account for the piezoelectric strain between differing materials, only being able to predict spontaneous polarization. These factors limit the reliability of XRD characterization for device analysis, so for this study, it serves only as a preliminary material assessment of films deposited by ALD.

### **2.3 Fabrication process**

The standard fabrication procedure for microelectronic devices (Fig. 2-3) involves depositing the relevant semiconductor nitride through ALD, then using sputter deposition to form the contact metal layer. A combination of UV lithography and wet metal etching are used to pattern the substrate, primarily the planar MOSCAP devices used to profile the heterojunction for substrate doping concentration, 2DEG concentration, and interface trap density. Other relevant characterization devices were also added, including transfer length method (TLM) structures for assessing contact quality through resistance and mobility measurements.

Sputtering uses a contact metal target which is repeatedly struck by inert gas particles in vacuum, in this process argon, to emit metal atoms from the target. These atoms then travel through the vacuum in random directions and slowly accumulate upon the sample surface. A planar magnetron source generates a strong magnetic and electric field perpendicular to each other. The resultant Lorentz force confines the electron plasma to a circular path on the target, vastly increasing the probability of impact ionization with argon and consequently, the amount of electrons and ions generated. In this study, chromium (Cr) and aluminum (Al) were used as the contact metals. The work function of Cr is 4.5 eV, which is high enough to produce a Schottky barrier with GaN, AlN, and ZrN<sub>x</sub>. In comparison, Al has a lower 4.1 eV work function [25], which is better suited for tunneling contacts as it forms a lower Schottky barrier with the aforementioned materials.

Photolithography is used to define the device areas on UV-sensitive photoresist for wet chemical etching. Positive photoresist (here HPR 504), which has increased solubility in developer solution after UV light exposure, is first spin coated on the metal layer. The device shapes are pre-written as opaque shapes on a transparent photomask, with which the area to be removed on the photoresist is selectively exposed to the UV lamp, then dissolved in developer solution (here Shipley Microposit 354). With the device areas now protected by photoresist, the samples are bathed in a chemical solution which has a high reaction rate with a specific metal compared to other materials. After the device pattern is transferred to the metal, the photoresist is removed by acetone. This process was used to fabricate the initial AlN/GaN MOSCAP devices on Cr metal as it is well-established and reliable. However, as mentioned in Section 2.1, it is not possible to pattern the polarization layer with wet metal etching, and thus the devices could not

be fully isolated from the rest of the mask. To correct this potential issue, lift-off was used to fabricate  $ZrN_x/GaN$ .

For lift-off deposition (Fig. 2-4), negative photoresist (here AZ 5214, developed using AZ 400K) is initially deposited on GaN. In contrast to positive photoresist, UV light exposure makes specific areas insoluble to developer solution. Thus, the lithography step defines a stencil layer in which the device areas are confined within the photoresist. The ultrathin semiconductor layer and contact metal are then deposited across the entire sample, with the devices filling up the interstitial areas of the photoresist. The photoresist, and with it, the metal/semiconductor area to be removed, is then dissolved in acetone solution, leaving the finished devices. As previously mentioned in Section 2.1, the low-temperature PEALD process allows thin films to be deposited on the photoresist without degrading it, and thus lift-off presents an effective method for patterning the films on GaN without using chemical etchants.

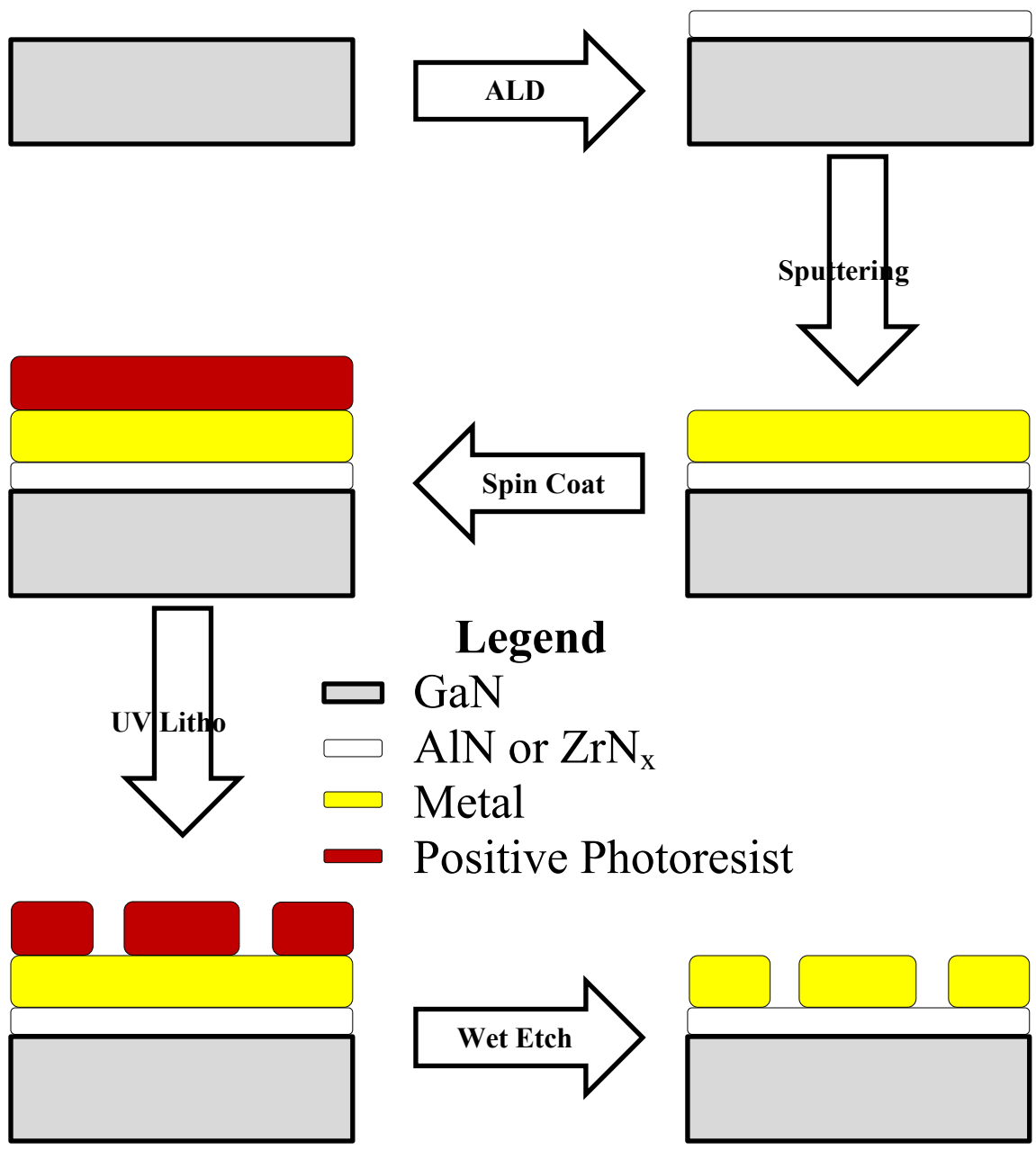


**Figure 2-3:** Metal etch patterning process flow.

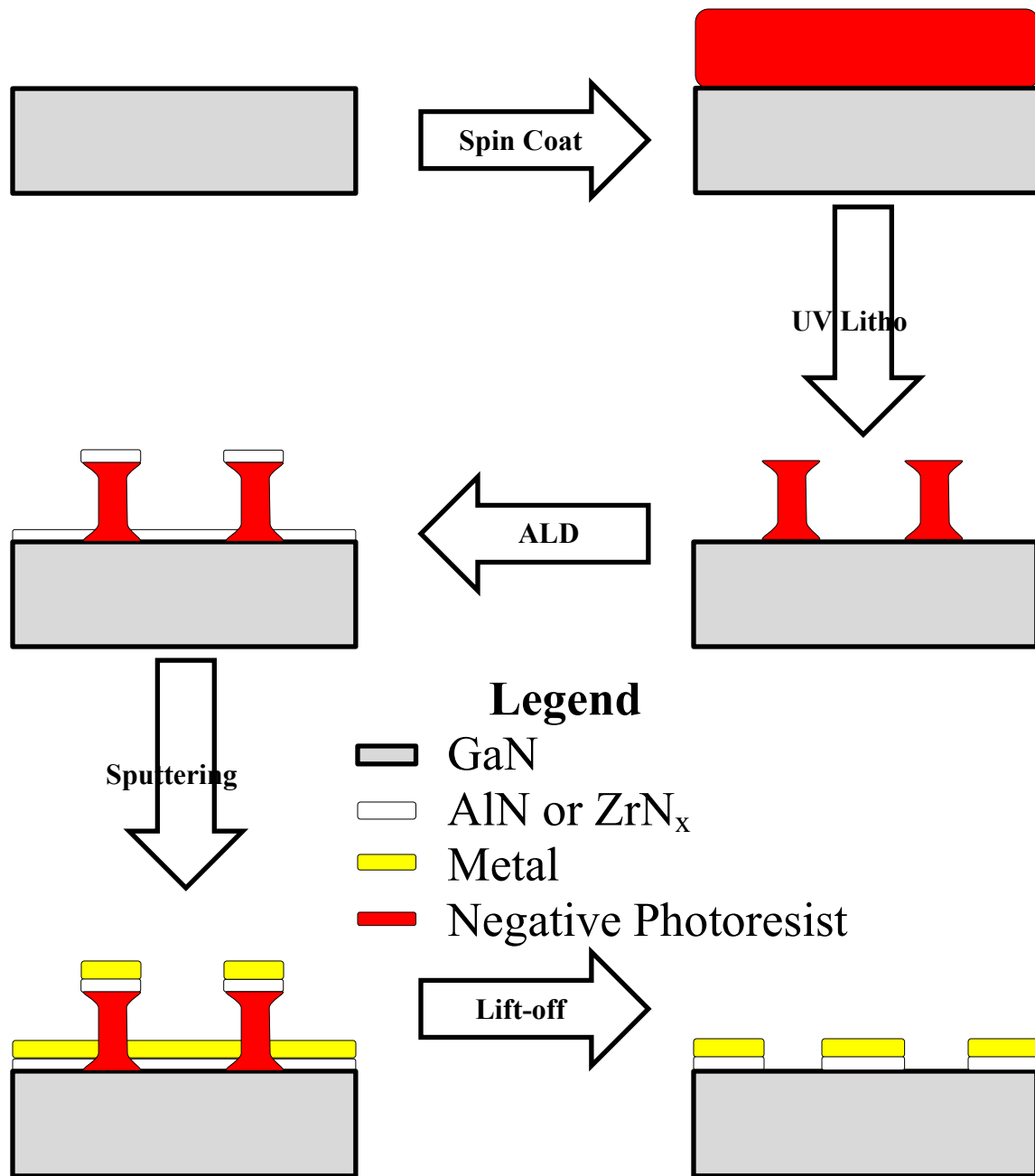
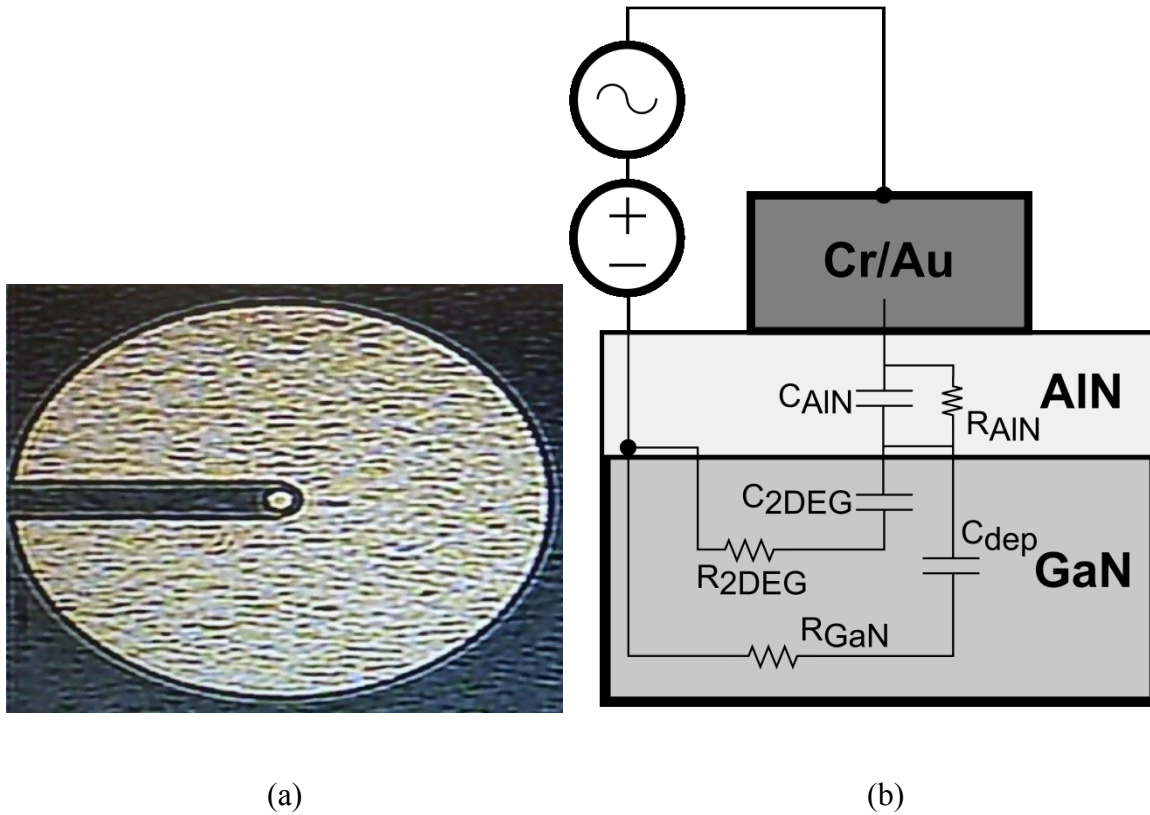


Figure 2-4: Lift-off deposition process flow.

## 2.4 MOSCAP and C-V profiling method



**Figure 2-5:** Planar MOSCAP (a) and equivalent circuit model [26,27] (b).

The planar MOSCAP shown in Figure 2-5 [26] is the device used to characterize the GaN heterojunction, consisting of two concentric circular contacts separated by a circumferential gap. The device can be expressed in a lumped-element RC circuit model in which current flows from the inner to the outer contact when stimulated by a forward voltage bias. The respective layer capacitances are  $C_{AIN}$ , which represents the polarization-induced dipole moment at the AlN layer, and  $C_{dep}$ , which represents the charge depletion layer at the GaN interface. The surface charge contribution to the measured capacitance, which includes the 2DEG underneath the accumulation layer and interface trap states, can be treated as parallel to the GaN depletion

capacitance. Capacitance-voltage (C-V) profiling can then be used to extract the 2DEG concentration.

C-V profiling [28] as a 2DEG measurement technique stems from the definition of capacitance as the change in electric charge with voltage:  $C=dQ/dV$ . For the reverse biased AlN/GaN MOSCAP structure, the 2DEG charge is steadily depleted from the interfacial quantum well, starting from the flat-band voltage  $V_{FB}$  which is indicated by the C-V inflection point around 0 V. This depletion, assuming minimal surface trap influence, is depicted by a capacitance plateau followed by a steep cut-off slope at a certain voltage  $V_C$ . The 2DEG concentration  $Q_n$  can then be found by integrating the capacitance over this gate voltage ( $V_G$ ) region using the formula:

$$Q_n = \int_{V_C}^{V_{FB}} C_{2DEG} dV_G \quad (2.2)$$

where  $C_{2DEG}$  is the 2DEG contribution to the total measured capacitance. This is calculated from the measured capacitance  $C_{Measured}$  as:

$$\frac{dQ_n}{dV_G} = C_{2DEG} \approx \left( \frac{1}{C_{Measured}} - \frac{1}{C_{AlN}} \right)^{-1} - C_{dep} \quad (2.3)$$

where  $C_{AlN}$  and  $C_{dep}$  are obtained through the respective formulas:

$$C_{AlN} = \frac{\epsilon_{AlN}}{t_{AlN}} \quad (2.4)$$

and

$$C_{dep} = \frac{1}{2} \sqrt{\frac{N_D q \epsilon_{GaN}}{V_{bi} - V}} \quad (2.5)$$

where  $t_{AIN}$  refers to the AlN thickness,  $N_D$  is the GaN doping concentration,  $q$  is the elementary charge, and  $V_{bi}$  is the built-in potential of the heterojunction.

Undesired surface state charging, which result from interface traps, is the primary contribution to capacitance measurement uncertainty. Acceptor-like traps, which capture electron charge, shift the flat-band and cut-off voltages to a more positive bias. In other words, the C-V curve moves to the right. Donor-like traps similarly capture positively charged holes and skew the curve leftward to a more negative bias [29]. These states charge depending on the small-signal measurement frequency [30]. The 2DEG measurements are taken at frequencies around 1 MHz due to the lower time constant permitted for surface state charging, which aids in mitigating these effects.

When the capacitance becomes very close to the thin film capacitance, the model breaks down since the series capacitance calculation leads to unreasonably high 2DEG values. Since substantial 2DEG is already required to reach these capacitances, the thin film capacitance is considered negligible in these cases.

C-V profiling offers greater measurement accuracy compared to methods such as Hall effect measurements, which use a perpendicular magnetic field to produce an electric field across the material and separate electron and hole charges. This is because it is an electrically-based measurement technique, which is non-destructive and avoids introducing noise effects such as magnetic flux. In addition, while the Hall effect isolates the charge from its original source, C-V profiling directly characterizes the charge distribution in the heterojunction depletion layer, and

thus it can more precisely determine the total charge contribution. These advantages make C-V profiling easily integrated with a standard device process flow.

The C-V profiling technique can also determine  $N_D$  through the formula:

$$N_D = -\frac{2}{q\varepsilon \frac{d(\frac{1}{C^2})}{dV}} \quad (2.6)$$

Thus, by taking the inverse square of the capacitance and plotting it against voltage ( $1/C^2$ -V),  $d(1/C^2)/dV$  is determined as the slope of the near-linear region trending towards 0 (Fig. 2-6). This can be substituted into Equation 5. Using this method, we have determined N+ GaN to have a doping concentration of approximately  $7 \times 10^{17} \text{ cm}^{-3}$  and N- GaN, shown in Fig. 2-6, to have a  $6 \times 10^{14} \text{ cm}^{-3}$  concentration. Both of these values are significantly less than the 2DEG concentration, which often surpasses a  $10^{20} \text{ cm}^{-3}$  bulk concentration in the polarization layer.

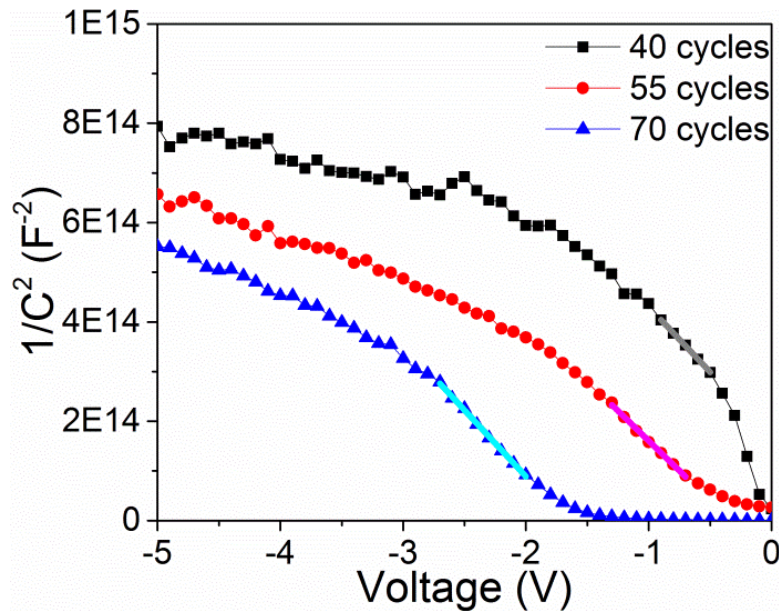


**Figure 2-6:**  $1/C^2$ -V plot for AlN (deposited with a various number of deposition cycles; see Chapter 3) on N- GaN. The highlighted areas represent  $d(1/C^2)/dV$ .

## 2.5 TLM and I-V profiling method

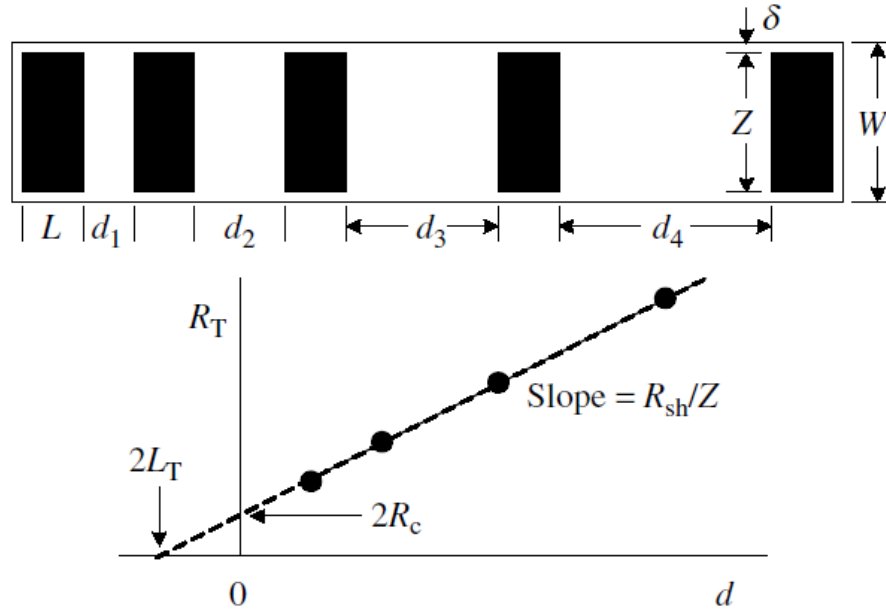


**Figure 2-7:** TLM structure (top) and plot indicating key resistance parameters (bottom) [30].

Current-voltage (I-V) plots are the most direct method of assessing contact quality since ohmic contacts are defined by their linear I-V characteristic. This can be measured through the MOSCAP structures, but transfer length method (TLM) structures are also used to measure key resistance parameters. Similar to the MOSCAP structures, they are modelled as lumped-element circuits (Fig. 2-7) [31,32]. The resistance in between TLM contacts ( $R_T$ ) can be measured from I-V plots and it varies linearly with their relative distance from each other. Key resistance parameters can thus be calculated from this relation. The contact resistance  $R_c$  can be extrapolated from the intercept, which represents both contacts fully overlapping each other and is equivalent by the formula  $2R_c$ . Similarly, the length for calculating the specific contact resistivity  $L_T$  can be extrapolated from the resistance intercept, though this calculation was not reported in this thesis as it is less accurate than the other two parameters. The slope represents

the resistance change with increased spacing, or the sheet resistance. This is equivalent to  $R_s/Z$ , with  $Z$  being the contact width. The sheet resistance can then be used to calculate the effective mobility  $\mu_{eff}$ . Its formula is given by:

$$\mu_{eff} = \frac{g_d L}{W Q_n} \quad (2.7)$$

where  $g_d$  is the conductivity, or  $1/R$ ,  $L$  is the contact length, and  $W$  is the width. Sheet resistance is given by the formula:

$$R_s = R \frac{W}{L} \quad (2.8)$$

and thus mobility can be expressed as:

$$\mu_{eff} = \frac{1}{R_s Q_n} \quad (2.9)$$

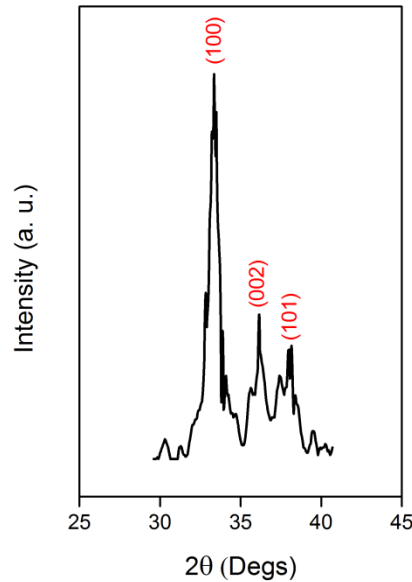
## 3 AlN/GaN

### 3.1 Overview

Due to the strong polarization strain between AlN and GaN, the heterojunction is highly sensitive to changes in AlN thickness within the nanometre range, leading to a narrow barrier width window for peak 2DEG and conductance. For maximum mobility in the AlN/GaN heterojunction, 3-4 nm was considered the target AlN thickness using MBE [15]. Thus, three different thicknesses were tested on each doping variation of GaN, using 40, 55, and 70 ALD cycles. Calculated from the deposition rate measured by ellipsometry in Section 2.1, these deposition parameters corresponded to 3.2 nm, 4.5 nm, and 5.7 nm respectively. The contact metal stack consisted of Cr/Au, each 100 nm thick and produced by wet etching, and GaN on sapphire was the wafer template. Although the 4 nm samples used Cr without Au, this would not significantly affect the measurements since Au was deposited on top of Cr, and thus does not diffuse into AlN or GaN.

According to the Matthews-Blakeslee theoretical model for piezoelectric polarization [12,13], an ideal heterojunction should remain fully strained with increasing AlN thickness for relatively thin layers. When it reaches a certain critical thickness, strain relaxation occurs and the 2DEG charge starts to decrease until only spontaneous polarization contributes to the 2DEG. For the AlN/GaN heterojunction, the model, adjusted by Fischer et al. [13], predicts 6 nm as the critical thickness [10]. C-V and I-V profiling were used to compare the 2DEG concentration and contact quality respectively over the 3-6 nm AlN thickness range. This encompasses the predicted optimal 2DEG window and approaches the strain relaxation onset, which allows for thorough investigation of polarization strain variation with respect to AlN thickness.

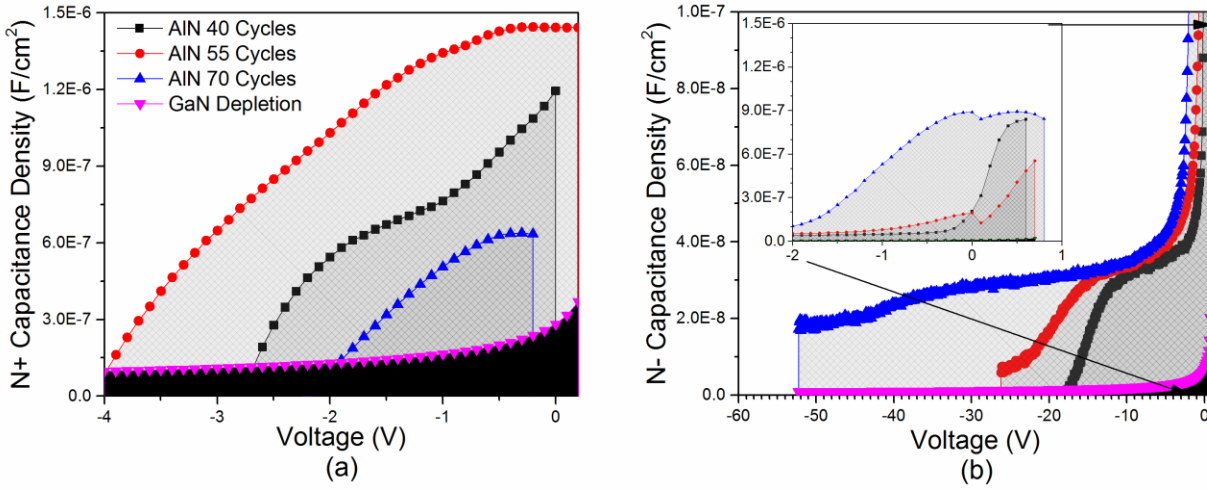
### 3.2 Crystallinity analysis



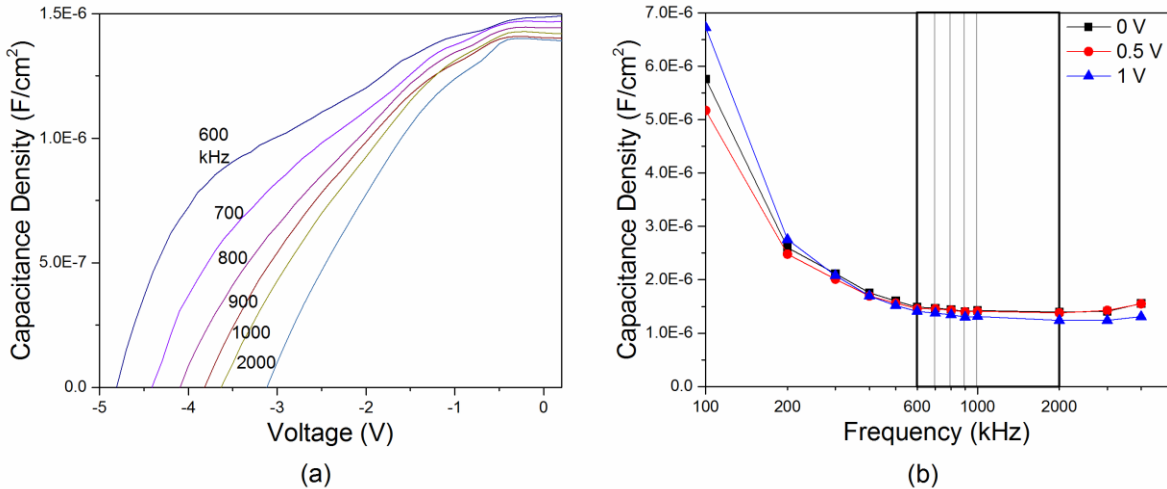
**Figure 3-1:** XRD plot for 20 nm AlN on Si(111) at 250°C deposition [33].

Fig. 3-1 shows the XRD plot for AlN on Si(111). The crystal structure of the layer is primarily oriented in the (100) direction instead of the (002) direction required for polarization. In addition, the significant amount of noise in the measurement indicates a small grain size and high defect concentration. These properties can be attributed to the low temperature deposition and consequently a lack of high-temperature annealing to improve the crystal quality. However, this plot is comparable to the plot shown by a similar study done at 185°C deposition temperature [34] and indicates that the AlN lattice structure is highly polycrystalline and hexagonal. Since it is difficult to perform XRD on <5 nm AlN, the layer's polarization interaction with GaN must be observed through electrical characterization. Nevertheless, the XRD demonstrates that low-temperature ALD can deposit AlN to near-epitaxial quality.

### 3.3 C-V Analysis



**Figure 3-2:** Comparison of directly measured C-V plots on (a) N+ and (b) N- GaN with 3-6 nm AlN thickness [33]. The black area represents the depletion capacitance calculated from Equation 2.5.



**Figure 3-3:** (a) Variation of C-V with frequency for 55 cycles of AlN on N+ GaN [33]. (b) Capacitance-frequency (C-F) plot of the data in (a) for 0-1 V. Highlighted is the minimum capacitance variation region.

Fig. 3-2 shows the C-V characteristics of the AlN/GaN heterojunction and their variation with respect to AlN thickness [33]. The N+ samples produce higher 2DEG charge overall, but are fully depleted at much lower voltages than the N- samples. For ideally sharp hetero-

interfaces with no deep defects, previous simulations [35] indicated that doping concentration should not have an effect on the 2DEG. As previously noted, surface state traps have a significant influence on the measurement. This indicates that deep defects arising from AlN deposition may have resulted in the differing C-V profiles, with their distribution varying by doping. Other factors include the lower Fermi level relative to the conduction band for N- GaN [36]. This would result in the 2DEG electrons being concentrated deeper into the quantum well, and thus it would require more energy to fully deplete the 2DEG. In addition, the bare surface barrier height (BSBH) is known to increase with lower doping concentration in GaN, from 0.6 eV for N+ GaN to 1.4 eV for N- GaN. This would imply a higher surface potential for the AlN/GaN heterojunction using N- GaN.

As shown in Figure 3-3, the N+ GaN samples demonstrate a high degree of capacitance variation among C-V plots measured from low to high frequencies [33]. The C-V cut-off slopes tend to be gradual due to a non-uniform interface trap distribution altering the measured capacitance [29,37]. This adds a high amount of uncertainty to the capacitance measurements. Consequently, the reported 2DEG was obtained by converting the C-V plots to capacitance-frequency around 0 V and locating the frequency at which minimum capacitance variation occurs, with frequency variation being the primary consideration in the reported error. In contrast to N+ GaN, N- GaN demonstrates little variation with respect to frequency, but the cut-off voltage may still shift as a result of the acceptor-like traps.

### 3.4 Band structure and 2DEG

Metal			AlN	GaN
$\Phi_{Cr}$	4.5 eV	$m^*$	0.27 <sup>a</sup>	0.2
$\Phi_{Al}$	4.1 eV	$\epsilon_r$ [8]	9	9.5
$E_x$	0.05 eV	$\chi_s$ (eV)	1.9 <sup>b</sup>	4.1 <sup>c</sup>
		$\Delta E_c$ (eV)	1.7	

<sup>a</sup>See Ref. [38]

<sup>b</sup>See Ref. [39]

<sup>c</sup>See Ref. [40]

**Table 3-1:** Simulation parameters of the AlN/GaN heterojunction.  $E_x$  refers to the electron emission energy and  $m^*$  refers to the effective mass.

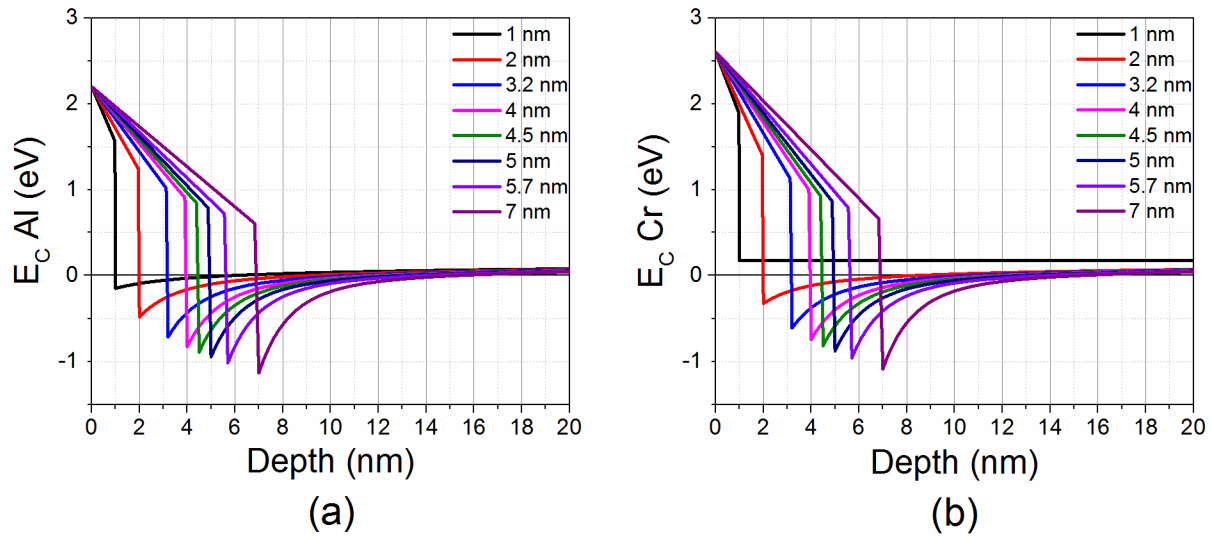


**Figure 3-4:** Band diagrams for the AlN/GaN for (a) Al contacts and (b) Cr contacts [27,33]. The N- GaN substrate assumed a  $6 \times 10^{14} \text{ cm}^{-3}$  doping concentration based on C-V doping profiling.

In order to compare the experimental 2DEG with the expected performance of an ideal AlN/GaN heterojunction, the energy band diagram for the AlN/GaN junction was modelled using a 1-D self-consistent Schrödinger-Poisson solver [41] using the parameters specified in Table 3-1. This sample assumed a fully strained AlN/GaN layer, and thus it could be used both to predict the 2DEG concentration at certain AlN thicknesses and indicate strain relaxation effects when

compared against the C-V profiled 2DEG concentration. Although a similar model has been shown in a previous work, this simulation was customized to more appropriately account for the specific sample parameters used in this work. Cao and Jena [15] assumed a 3.0 eV Schottky barrier height since they found that barrier heights less than 2.0 eV overestimated their 2DEG charge measured. This is higher than the theoretical height for the contact metals used in our sample with AlN. Thus, the barrier height was lowered to 2.6 eV and 2.2 eV respectively for Cr and Al.

Although the difference in electron affinity between AlN and GaN implies a band offset of 2.1 eV, the previous analysis has shown that the unstrained AlN/GaN offset tends to overestimate the 2DEG, since band gap shrinking occurs due to polarization-induced biaxial tensile strain. As a result, this simulation uses the adjusted 1.7 eV [15].

As shown in Fig. 3-4, the interface quantum well deepens with increasing AlN thickness due to stronger polarization strain, leading to the expected logarithmic increase [10] in 2DEG concentration shown in Fig. 3-5. The theoretical 2DEG concentrations are compared against the 2DEG concentrations obtained by C-V profiling, specifically by integrating the capacitance over the voltage range highlighted in Fig. 3-2. The simulated curve is close to the upper limit of the 2DEG uncertainty for 3.2 and 4.5 nm of AlN on N<sup>+</sup> GaN, which shows that it serves as a reasonable approximation of the maximum possible 2DEG at certain AlN thicknesses. The change in band diagram was found to be insignificant when the GaN doping was raised to  $7 \times 10^{17} \text{ cm}^{-3}$ , which is likely because the AlN/GaN band offset is much higher than the Fermi level adjustment with doping concentration. This hints at band structure differences arising from varied GaN doping, likely due to surface-state pinning by acceptor-like traps.

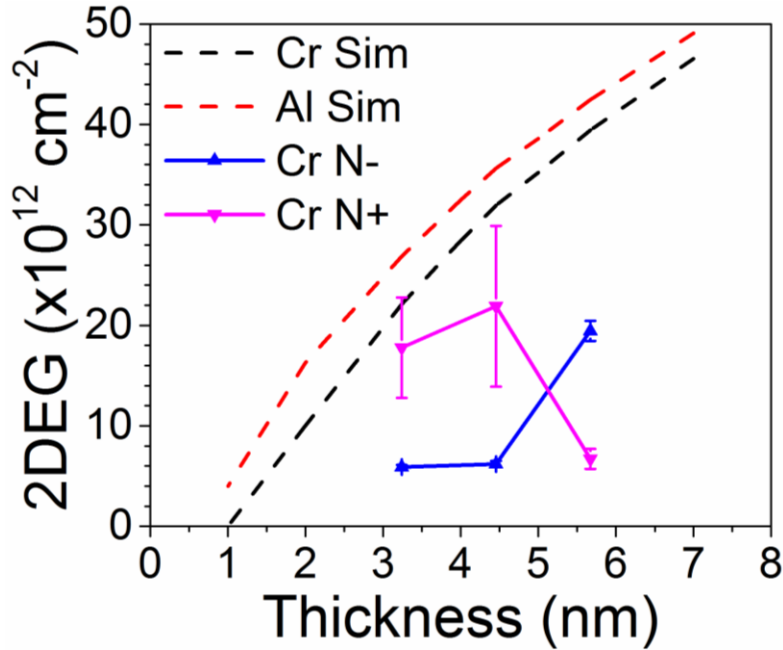


**Figure 3-5:** Comparison of experimental 2DEG with simulations for Cr and Al contact metals [27,33].

ALD cycles	Thickness (nm) <sup>a</sup>	Doping	$V_{FB}$ (V)	$Q_n$ ( $\times 10^{12} \text{ cm}^{-2}$ ) <sup>b,c</sup>	T	$Q_T$ ( $\text{cm}^{-2}$ ) <sup>d</sup>
40	3.2	N-	0.6	$5.9 \pm 0.2$	$1.64 \times 10^{-11}$	97
		N+	0	$18 \pm 5$		290
55	4.5	N-	0.7	$6.2 \pm 0.3$	$4.62 \times 10^{-16}$	0.00029
		N+	0.2	$22 \pm 8$		0.012
70	5.7	N-	0.8	$19 \pm 1$	$2.04 \times 10^{-18}$	$4.1 \times 10^{-5}$
		N+	-0.2	$7 \pm 1$		$1.4 \times 10^{-5}$

**Table 3-2:** Summary of MOSCAP CV results for the AlN/GaN junctions, compared with simulated transmission coefficients [33].

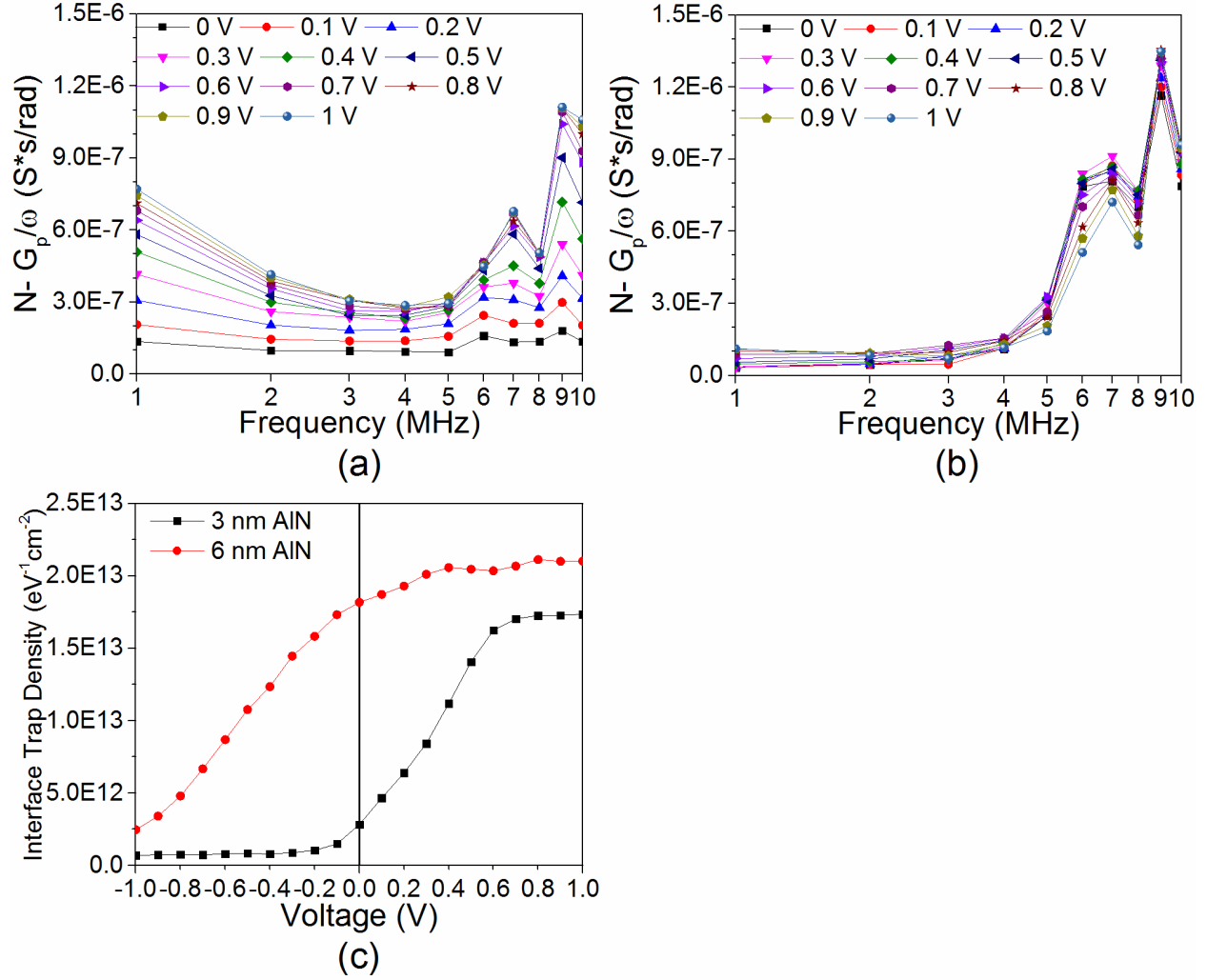
In addition, Fig. 3-4 indicates that using Al contact metal instead of Cr would result in deeper quantum wells and consequently, higher 2DEG concentrations (Fig. 3-5) due to its lower work function. This may aid in improving conductance through the AlN barrier. The effects of replacing Cr with Al will be discussed in Section 3.5.

Table 3-2 shows the experimentally observed 2DEG concentrations [33]. The 2DEG peaks at 55 cycles for N+ GaN and 70 cycles for N- GaN, indicating maximum piezoelectric polarization near those points. It has been theorized that the sudden rise in 2DEG concentration at a certain critical thickness can be attributed to the strain relaxation onset. The large concentration drop for 70 cycles of AlN on N+ GaN lends credence to that theory. As Fig. 3-5 shows, this thickness changes with doping concentration. The strain relaxation onset occurs at a thinner AlN layer than predicted by the Fischer model with N+ GaN; around 4.5 nm instead of 6 nm. In contrast, N- GaN does display the relaxation onset near the expected thickness or greater.

The abrupt increase in 2DEG with thickness for N- GaN contradicts the simulated predictions and the trend set by N+ GaN, since strain relaxation occurs at layers thinner than 70 cycles, the thickness at which peak 2DEG is achieved. This anomalous behaviour indicates a high concentration of acceptor-like traps at the AlN surface, which may have resulted from the low-temperature deposition process. Specifically, the XRD data suggests a high defect concentration which has not been repaired through post-deposition annealing. This theory was tested through the relation of the interface trap concentration  $Q_{it}$  to the threshold voltage  $V_{th}$ , given by the equation [42]:

$$V_{th} = \frac{\phi_b}{q} - \frac{\Delta E_C}{q} + \frac{E_{f0}}{q} - \frac{qd_{AlN}}{\epsilon_{AlN}}(Q_n + Q_{it}) \quad (3.1)$$

Since the simulated 2DEG concentration assumes a fully strained heterojunction,  $Q_{it}$  was calculated as the difference between the theoretical and measured 2DEG.  $G_p/\omega$ -F plots (Fig. 3-6) were used to determine the interface trap density  $D_{it}$  according to the formula [43]:



**Figure 3-6:** Conductance-frequency ( $G_p/\omega$ -F) plots normalized with respect to frequency for (a) 40 cycles of AlN on N- GaN and (b) 70 cycles on N- GaN.  $D_{it}$  is derived from the local maximum near the highest frequency (9 MHz), which is measured and integrated over -1 – 1 V to calculate  $Q_{it}$  (c).

$$D_{it} = \frac{2.5}{q} \left( \frac{G_p}{\omega} \right)_{max} \quad (3.2)$$

From this equation, the interface trap concentration can be derived using the equation

[44]:

$$Q_{it} = -q^2 \int D_{it} d\phi_s \quad (3.3)$$

ALD Cycles	Thickness (nm)	Simulation			Experimental	
		$Q_n$ ( $\times 10^{12} \text{ cm}^{-2}$ )	$Q_{it}^a$ ( $\times 10^{12} \text{ cm}^{-2}$ )	$V_{th}$ (V)	$Q_n$ ( $\times 10^{12} \text{ cm}^{-2}$ )	$Q_{it}$ ( $\times 10^{12} \text{ cm}^{-2}$ )
40	3.2	22	16	-0.4	$5.9 \pm 0.2$	13
55	4.5	32	26	-1.8	$6.2 \pm 0.3$	N/A <sup>b</sup>
70	5.7	39	20	-3.4	$19 \pm 1$	30

<sup>a</sup>Calculated as the difference between simulated and experimental 2DEG.

<sup>b</sup>Interface trap density could not be obtained for 55 cycles.

**Table 3-3:** Comparison of AlN trap charge and threshold voltage with thickness on N- GaN. Surface charge sources apart from the 2DEG and interface traps are treated as negligible.

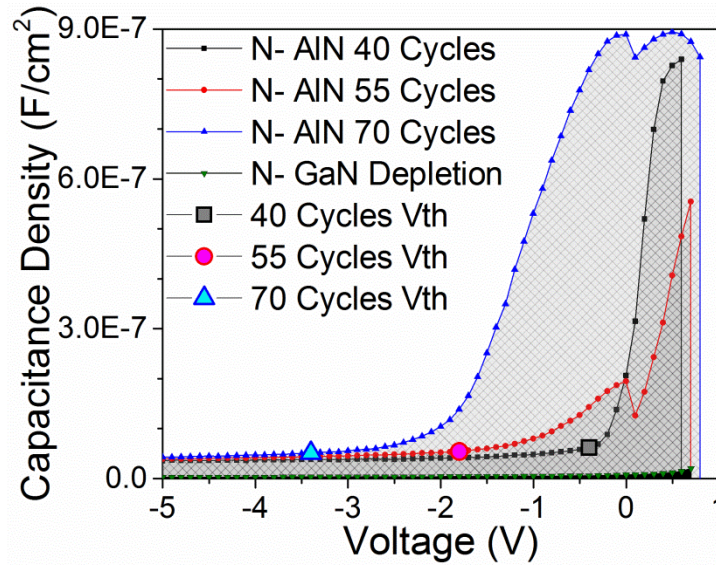


**Figure 3-7:** C-V plots of AlN on N- GaN near 0 V, highlighting the  $V_{th}$  locations calculated from Equation 3-6.

where  $\phi_s$  is the AlN/GaN surface potential.

From the estimated  $Q_{it}$  values,  $V_{th}$  was calculated for each thickness of AlN (Table 3-3) using Equation 3.1. These predicted  $V_{th}$  values highlighted in Fig. 3-7 are located near the onset of rising capacitance for each C-V curve, and thus the expected  $Q_{it}$  closely agrees with the C-V measurements. This result demonstrates evidence that acceptor-like surface states are the primary cause of the lowered 2DEG charge measurements in the AlN/N- GaN heterojunction compared

to the theoretical concentration at full polarization strain. Although 70 cycles of AlN generates a higher interface trap concentration compared to 40 cycles, it retains a higher 2DEG concentration due to its stronger piezoelectric polarization with GaN.

To confirm this theory, the theoretical  $Q_{it}$  values were compared to the measured  $Q_{it}$  from the plots in Fig. 3-6. The  $D_{it}$  was determined through Equation 3.2, using the plots in Fig. 3-6a and 3-6b as reference, and  $Q_{it}$  was calculated through Equation 3.3 by integrating  $D_{it}$  over the surface potential, assumed to be over the  $-1 - 1$  V range shown in Fig. 3-6c. Although this does not completely represent the total band gap energy range, the  $Q_{it}$  calculated for 3 nm of AlN is close to theoretical prediction. Also as predicted, 70 cycles of AlN shows a higher  $Q_{it}$ , although it may be overestimated since the sum of it and the 2DEG is much higher than the total polarization charge indicated in the simulation. The  $G_p/\omega$ -F measurements will need to be taken at a greater voltage range to more accurately assess the  $Q_{it}$ . Nevertheless, these results demonstrate a high contribution of interface trap to the total AlN/N- GaN charge, which shows further evidence that 2DEG charge is being lost to acceptor-like trap states.

Overall, before the strain relaxation onset, N+ GaN demonstrates higher 2DEG concentrations and a lower critical thickness than N- GaN, indicating that piezoelectric polarization occurs to a greater degree. This seems to indicate crystal growth differences in AlN with varying doping concentrations of GaN, with higher doping leading to a greater degree of crystallinity. The high defect concentration and relatively weak polarization in N- GaN reflects a highly polycrystalline interface. Thus, achieving high 2DEG with N- GaN requires a thicker AlN layer than N+ GaN when using low-temperature ALD to apply the layer.

### 3.5 Quantum tunneling and I-V analysis

Although high 2DEG concentrations are favourable for consistent electron transmission, the transmission probability potentially has a greater influence on how effectively the electrons are transported through the AlN barrier. To predict the degree of quantum tunneling occurring in the AlN/GaN samples, the potential diagrams in Figure 3-4 were used to plot the transmission coefficient through the AlN barrier as shown in Fig. 3-8 [27]. This was calculated from a multistep potential barrier model using a 1-D mesh calculation of the wave function at multiple specific intervals [45]. For band diagrams with abrupt energy changes, it is considered more accurate than the WKB approximation. The transmission coefficient demonstrates an exponential relation with AlN thickness, decreases by a factor of  $\sim 10^3$  per nanometre increase. Using a higher Schottky barrier at the metal-AlN interface reduces the rate of decline. Thus, Al contacts are favoured for maximizing conductance, since it results in both higher 2DEG and a lower energy barrier that encourages greater thermionic emission as well as quantum tunneling.

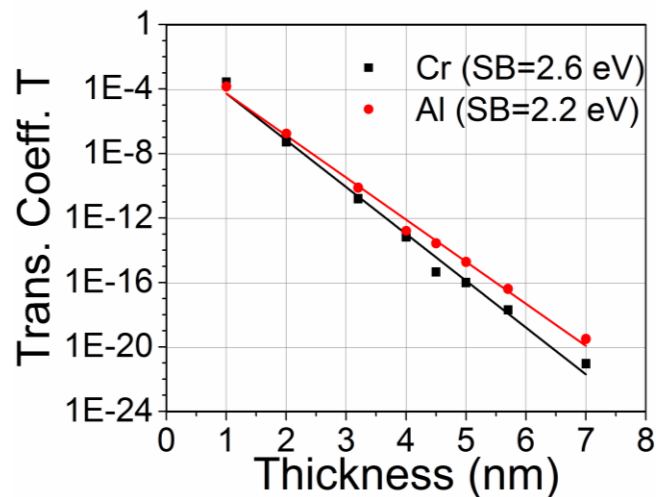


**Figure 3-8:** Logarithmic plot of transmission coefficient against thickness for the band diagrams in Figure 3-7 [27].

The average number of 2DEG electrons tunneling through the AlN layer can be expressed as the product of the 2DEG concentration and transmission coefficient [27]. From Table 3-2, the sample with 40 cycles of AlN on N- GaN shows a notable amount of charge being transmitted while higher thicknesses result in significantly reduced transmission. From this result, we can predict that around 3 nm, consistent quantum tunneling can be obtained. This prediction only considers transmission through the undoped ideal AlN layer shown in Fig. 3-4. Other factors that affect the transmission coefficient that were not considered include interface state tunneling and other conduction mechanisms.

Current-voltage plots for the AlN/GaN junction are shown in Fig. 3-9. Like the C-V plots, the I-V plots demonstrate different current characteristics with doping [27]. The N+ GaN samples display pseudo-ohmic characteristics across 40-70 cycles of AlN, with the thickest layer sample being more resistive than the other samples due to strain relaxation. Despite the thicker barrier, 55 cycles produced the most conductive and linear plot compared to 40 and 70 cycles. This is likely due to its high bulk donor concentration, which provides an additional electron source for quantum tunneling through AlN and thus promotes more consistent current flow.

A pseudo-ohmic curve is only achieved on N- GaN when AlN is 40 cycles thick, as higher thicknesses result in a non-ohmic curve. This behaviour is to be expected based on the simulations since the transmission coefficient, and thus, the predicted tunneling charge, is highest at 3 nm. In addition, due to their lower donor concentration, fewer charge carriers exist in the bulk GaN layer, drastically reducing the overall current compared to N+ GaN.

The temperature-dependent I-V plots shown in Fig. 3-10 further illustrate differences in ohmic behaviour, since higher temperatures correlate to increased electron energy for thermionic

emission. For 40 cycles of AlN on N+ GaN, the conductivity is minimally temperature dependent, but with the thickness increased to 55 cycles, the I-V curve becomes increasingly linear up to 100 C. A similar effect is displayed for 40 cycles on N- GaN. The latter two samples demonstrated the most linear I-V curves of their respective doping concentrations indicating a high degree of electron transmission through both thermionic emission and quantum tunneling.

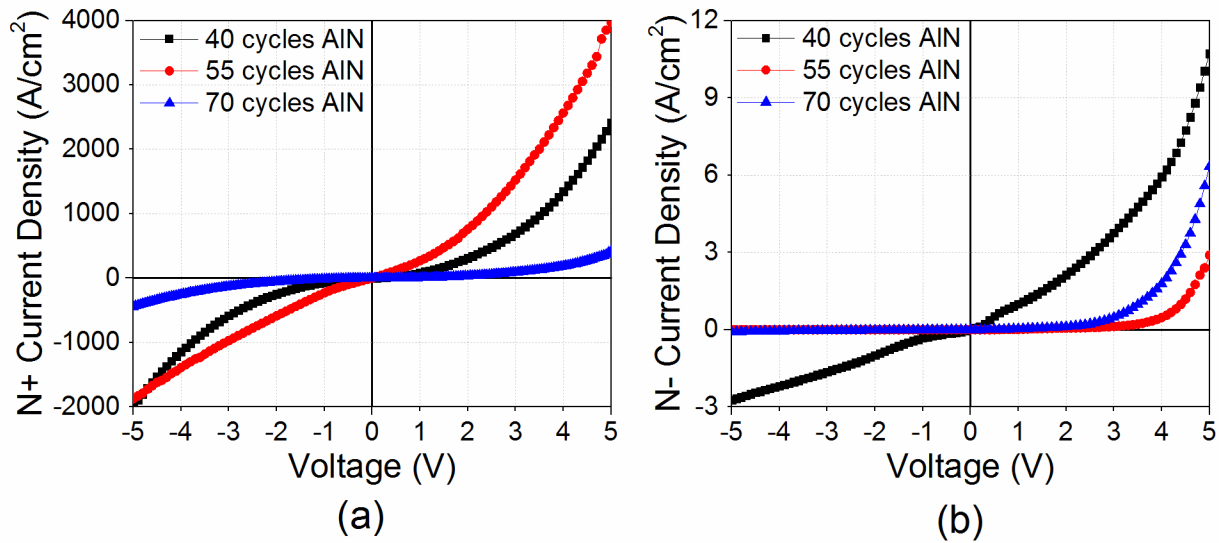


**Figure 3-9:** Current density measurements for (a) N+ GaN and (b) N- GaN [27].

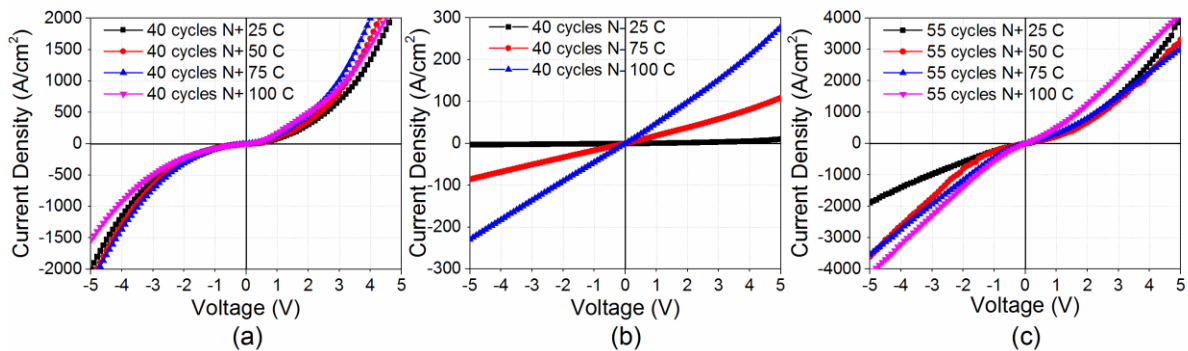


**Figure 3-10:** Effect of temperature on current density curves for (a) 40 cycles of AlN on N+ GaN, (b) 40 cycles on N- GaN, and (c) 55 cycles on N+ GaN [27].

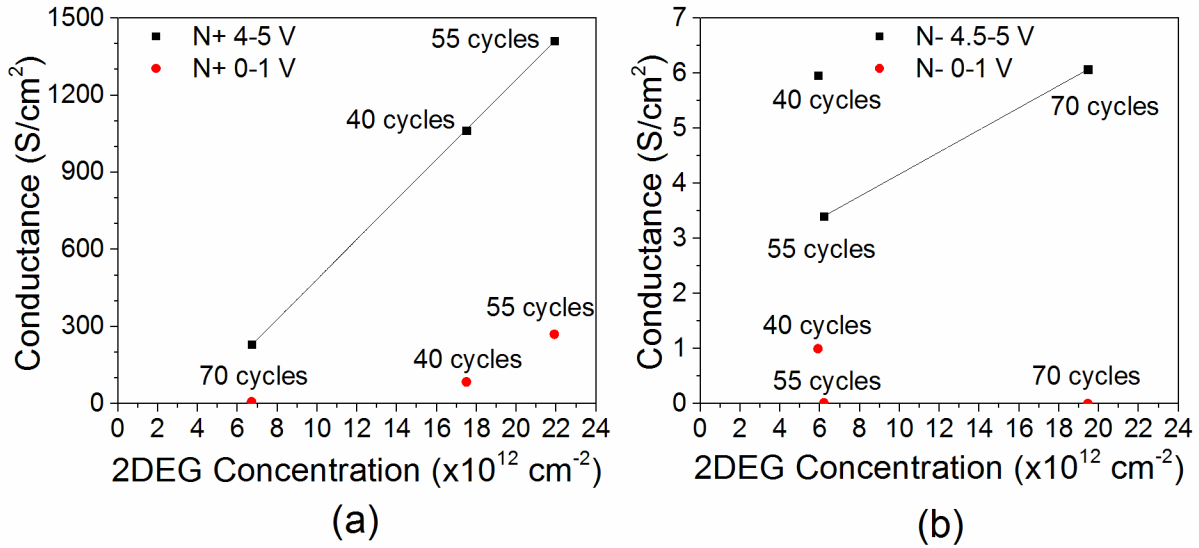


**Figure 3-11:** Comparison of conductance (derived from the I-V slopes) to 2DEG concentration for (a) N+ GaN and (b) N- GaN [27].

By comparing the conductivity of the I-V plots with 2DEG as shown in Fig. 3-7, the change in I-V behaviour with doping becomes more apparent [27]. At low voltages, 55 cycles of AlN on N+ GaN results in an above average conductivity compared to the other samples, while conductance is minimal for samples with more than 40 cycles of AlN on N- GaN. At higher voltages, 2DEG and conductance form a near-perfect linear relation for N+ GaN, while 40 and 70 cycles on N- GaN have comparable conductivity values due to the higher 2DEG produced by the latter sample. This shows that the linearity of the N+ GaN I-V plots is minimally affected by thickness, and the 2DEG concentration is the primary influence on the AlN transmission probability since the high electron donor concentration helps promote a constant flow of electrons. In contrast, N- GaN has a much lower donor concentration, and thus the tunneling probability becomes more exponentially dependent on the AlN barrier thickness. However, at higher voltages, the greater 2DEG concentration for 70 cycles of AlN also becomes a

contributing factor. Both of these trends can serve as a guideline for predicting the behaviour of AlN/GaN contacts fabricated using low-temperature ALD.

Due to the high 2DEG and conductance achieved with 40 cycles of AlN on N+ GaN, TLM measurements were taken on the sample to determine its key resistance parameters. Fig. 3-12 shows the sample's resistance, derived from I-V slopes, compared to TLM contact spacing, for both Cr and Al contacts [33]. Table 3-4 shows the extracted contact resistance, sheet resistance, and mobility derived from the TLM method. While using Al contacts does not significantly impact sheet resistance and mobility, it greatly improves the contact resistance to

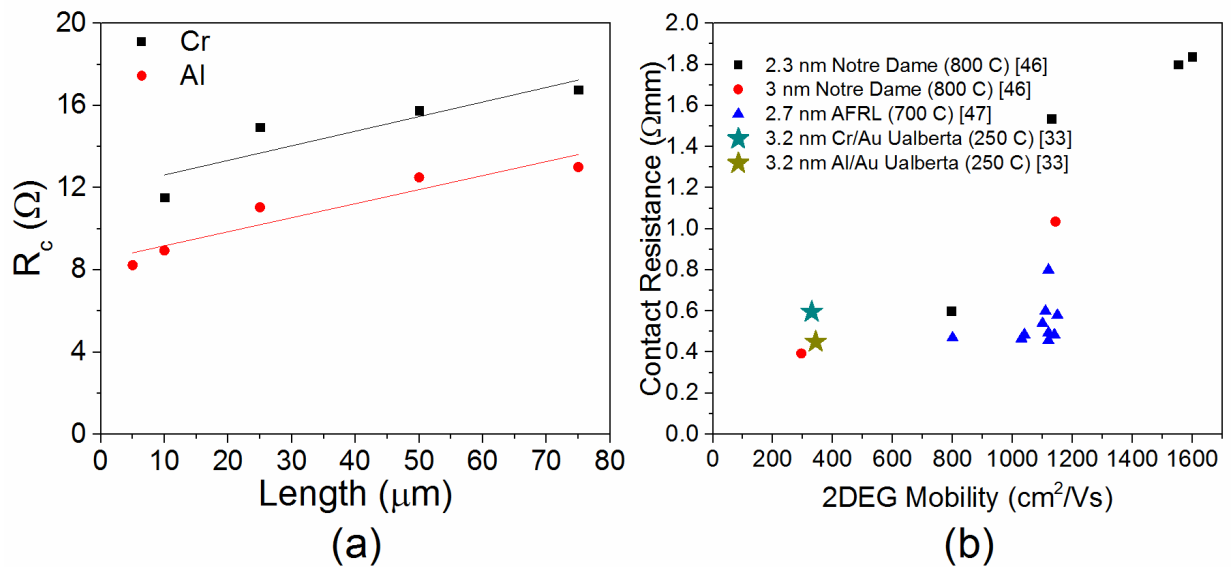


**Figure 3-12:** TLM characterization of 40 cycles of AlN on N+ GaN, with regards to (a) resistance as a function of TLM spacing and (b) comparison of contact resistance with mobility against similar studies [33]. The resistance in (a) was derived from the I-V slopes.

Contact	$R_c$ ( $\Omega \cdot \text{mm}$ )	$R_c$ ( $\Omega \cdot \text{cm}^2$ )	$R_s$ ( $\Omega/\text{sq}$ )	$\mu_{\text{eff}}$ ( $\text{cm}^2/\text{Vs}$ )
Cr/Au	0.606	$3.0 \times 10^{-4}$	355	330
Al/Au	0.45	$2.2 \times 10^{-4}$	341	343

**Table 3-4:** TLM-derived resistance and mobility for the sample in Fig. 3-10 for both contact metals under test [33].

levels comparable to other processes using molecular-beam epitaxy (MBE) (Fig. 3-12b [46,47]) while reducing the process temperature from at least 700°C to 250°C. Though measurements show a high sheet resistance and low mobility, this may be a result of increased surface roughness as lower contact resistances tend to correlate to lower mobility values.

Another factor contributing to the lower velocity is the use of trimethylaluminum instead of pure aluminum as the ALD precursor. It has the chemical formula  $\text{Al}_2(\text{CH}_3)_6$ , which has an atomic weight of 144.2 g/mol compared to elemental aluminum's 26.98 g/mol. The thermal velocity  $v_{th}$  as a result of process temperature can be compared using the formula:

$$v_{th} = \sqrt{\frac{k_B T}{m}} \quad (3.3)$$

where  $k_B$  is the Boltzmann constant,  $T$  is the process temperature, and  $m$  is the precursor mass. For this process, the thermal velocity is reduced by a factor of 3.87 compared to the 700°C MBE process with pure aluminum precursor.

Overall, low-resistance ohmic contact behaviour has been achieved for around 3.2 nm of AlN on N+ GaN using Al contacts. These parameters will aid GaN MOSFET development with minimal contact degradation. In addition, the low process temperature enables the use of lift-off deposition to selectively pattern AlN, thus enabling selective integration of these low-resistance contacts specifically into the highly doped source/drain contact areas.

### 3.6 Effects of annealing on N- GaN

Anneal Temperature (°C)	Anneal Time (s)	Conductance (S/cm <sup>2</sup> ) <sup>a</sup>
25	30	0.025
400	30	0.027
500	30	0.11
700	~120	222
900	30	5.1

<sup>a</sup>Derived from the I-V curves in Fig. 3-13

**Table 3-5:** Variation of 0 V conductance with annealing temperature for 40 cycles of AlN on N-GaN.

Although high conductance has been consistently achieved using AlN on N+ GaN, the current output of AlN on N- GaN is very low in comparison. As explained in Section 3.4, this is likely due to the high defect concentration present. Annealing was thus performed on the N- GaN samples with the intent of repairing the damage done to the AlN/GaN interface as a result of the low-temperature ALD process. The samples were heated in a three-zone furnace at temperatures ranging from 400°C – 900°C for 30 s, although the 700°C anneal was extended to approximately 2 minutes.

Table 3-5 compares the conductance at 0 V for the varying annealing temperatures on 40 cycles of AlN on N- GaN. While the conductance changes minimally from 400-500°C, the peak conductance attained at 700°C improves over the room temperature conductance by a factor of  $10^4$ . The longer annealing time may have also contributed to the higher conductance, since a sharp drop in conductance for the higher 900°C annealing. This suggests that 30 s is insufficient for annealing AlN/GaN and that longer annealing times are favoured.

Starting from 700°C, the C-V plot could not be obtained for the device due to its high conductance, which is expected from MOSCAP model analysis. As Fig. 2-5 shows, the AlN

resistance  $R_{\text{AlN}}$  is coupled in parallel with the AlN capacitance. When  $R_{\text{AlN}}$  is particularly low, as it is after  $>700^{\circ}\text{C}$  post-deposition annealing, it creates a short circuit from which the capacitance cannot be accurately determined from direct measurements. Thus, the variation in 2DEG with annealing temperature is currently unknown.

The high conductance achieved after post-deposition annealing shows promise towards improving the low current output of AlN on N- GaN, and this study suggests that the ideal annealing parameters are an annealing time of more than 1 minute and a furnace temperature around  $700^{\circ}\text{C}$ . Further experiments will be conducted using TLM structures to obtain the contact and sheet resistance.

## 4 Semiconducting $ZrN_x/GaN$

### 4.1 Overview

Reliability issues currently facing GaN devices, including gate leakage and current collapse, primarily result from the high electric field generated at the drain-side gate edge of GaN devices (Fig. 4-1) [48]. As previously mentioned in Section 1.5, AlN has a low capacity for electrical and thermal breakdown, which makes it a poor material for operating within this region. Thus, this chapter outlines the investigation of  $ZrN_x$  as a possible alternative polarization layer material for achieving 2DEG and low-contact resistance. Since our reliability tests outlined in Section 1.5 have demonstrated vast improvements in predicted lifetime operation and breakdown field compared to AlN,  $ZrN_x/GaN$  is worth investigating as a potential ohmic contact within the high-field region of the GaN MOSFET.

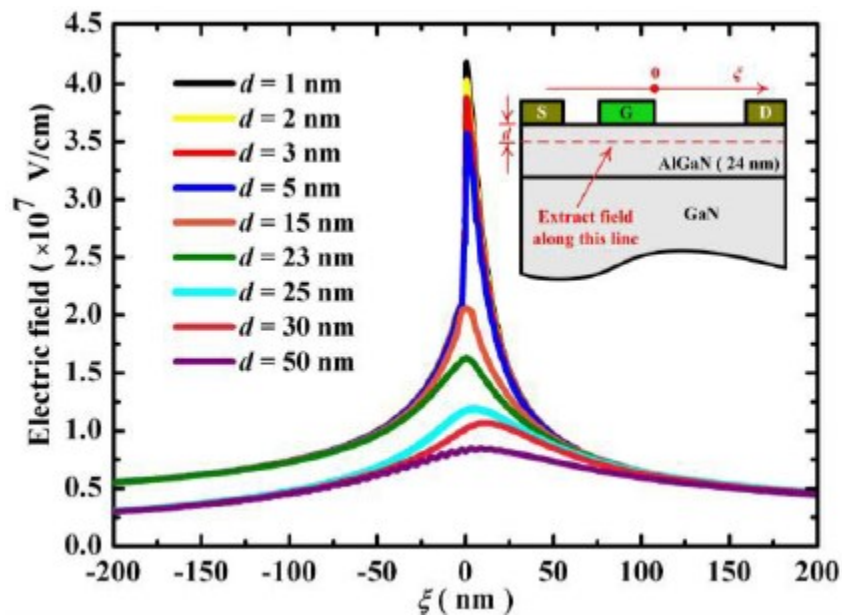


**Figure 4-1:** Simulated AlGaIn/GaN HEMT electric field distribution with respect to vertical and lateral distance [48]. The origin is set at the drain-side gate edge.

## 4.2 Band structure predictions

The work function of ZrN was previously reported at 4.2-4.6 eV [49] depending on nitride concentration. This value is comparable to the Cr and Al metal work functions and the GaN electron affinity, which implies a closely matched conduction band structure between ZrN and GaN. Compared to AlN/GaN, this would result in a reduced band offset with GaN and a lower Schottky barrier with metal contacts. Thus, ohmic contacts would be theoretically easier to produce with ZrN/GaN. To verify this prediction, the ZrN<sub>x</sub>/GaN band diagram was calculated through a Schrödinger-Poisson solver (Fig. 4-2), assuming a 4.0 eV electron affinity for ZrN<sub>x</sub> and a 0.13 eV band offset between the two materials (Table 4-1). These parameters were experimentally obtained through C-V profiling of ZrN<sub>x</sub>/GaN, since work functions and electron affinities often change due to processing differences.

The Fermi level is known to rise relative to the GaN conduction band with higher n-type doping levels. This effect was negligible for AlN/GaN due to the high band offset, but for ZrN<sub>x</sub>/GaN, the Fermi level adjustment with doping has a more pronounced effect. For N<sup>+</sup> GaN, the triangular quantum well is positioned slightly above the Fermi level, and the simulation predicts a low ( $<1 \times 10^{12} \text{ cm}^{-2}$ ) 2DEG concentration with minimal change with respect to ZrN<sub>x</sub> thickness. The 2DEG concentration would be even lower for N<sup>-</sup> GaN, as its conduction band is significantly higher than the Fermi level. In both cases, the quantum well seems to become slightly deeper with decreased ZrN<sub>x</sub> thickness, which implies that peak performance would be achieved with the thinnest barrier possible.

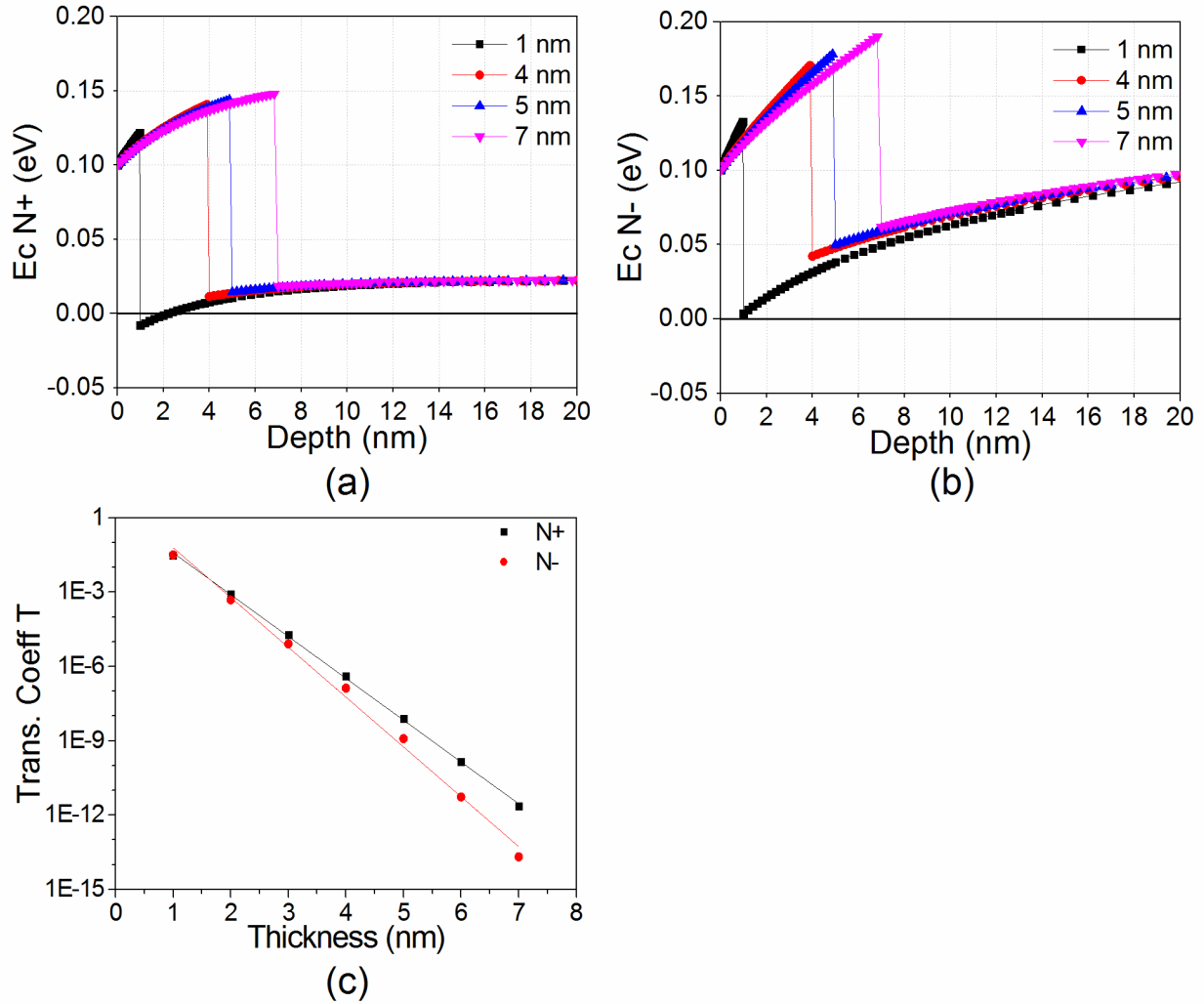


**Figure 4-2:** Simulated band diagrams for 1-7 nm of ZrN<sub>x</sub> on (a) N+ GaN and (b) N- GaN. The transmission coefficient with respect to ZrN<sub>x</sub> thickness is shown in (d).

Metal			ZrN <sub>x</sub>	GaN
$\Phi_{Cr}$	0.5 eV	$m^*$	1.55	0.2
$\Phi_{Al}$	0.1 eV	$\epsilon_r$	3.5	9.5
$E_x$	0.05 eV	$\chi_s$	4.0	4.1
		$E_c$	1.30E-01	

**Table 4-1:** Simulation parameters for the ZrN<sub>x</sub>/GaN heterojunction.

Thickness (nm)	Metal	Doping	Trans. Coeff T
7	Cr	N+	5.3E-24
		N-	3.4E-27
	Al	N+	2.3E-12
		N-	2.1E-14

**Table 4-2:** Comparison of simulated transmission coefficient with varying contact metals and spacing, derived from Fig. 4-1c and 4-1d.

Both Cr and Al were tested as possible contact metals, leading to significantly different band diagrams for a 0.4 eV Schottky barrier change. For Cr, the conduction band bends downward, with no quantum well formed, while Al contacts lead to a small well. This discrepancy is observed due to the low band offset. With Cr, the Schottky barrier is higher than the offset, and thus the  $ZrN_x$  conduction band does not bend below GaN. Thus,  $ZrN_x/GaN$  displays a low transmission probability (Table 4-2). With Al, transmission is more favourable due to the lower barrier height across  $ZrN_x$ , and thus it better facilitates electron transmission. As Fig. 4-1d shows, it displays an approximately 100 times lower transmission coefficient with each nanometre increase in  $ZrN_x$  thickness compared to the 1000 times lower coefficient decrease per nanometre for AlN/GaN. Despite the low predicted 2DEG, the high transmission coefficient should allow ohmic contacts to form for 1-7 nm of  $ZrN_x$ .

The simulation presented in this section only outlines for initial predictions of the band structure, since the material properties of  $ZrN_x$  are not fully understood. Further speculations of the band structure are presented through C-V and I-V electrical characterization in the following sections.

## 4.2 Elemental composition of $ZrN_x$

Following the experiment previously performed on the AlN/GaN samples in Chapter 3, MOSCAP structures consisting of 1-7 nm thick  $ZrN_x$  layers on GaN were fabricated using PEALD for characterization through C-V and TLM profiling. X-ray photoelectron spectroscopy (XPS) was used to determine the chemical composition of the  $ZrN_x$  layers, with the elemental peaks being shown in Fig. 4-3. From the percent concentrations shown in Table 4-3, the nitrogen concentration in  $ZrN_x$  was found to be  $x=1.15$ , which is near the middle of metallic ZrN and insulating  $Zr_3N_4$ . Thus, the material was predicted to display semiconducting behaviour. Also present in  $ZrN_x$  are substantial carbon (C) and oxygen ( $O_2$ ) contaminants, which would form insulating ZrC and  $ZrO_2$  when bonded with Zr.

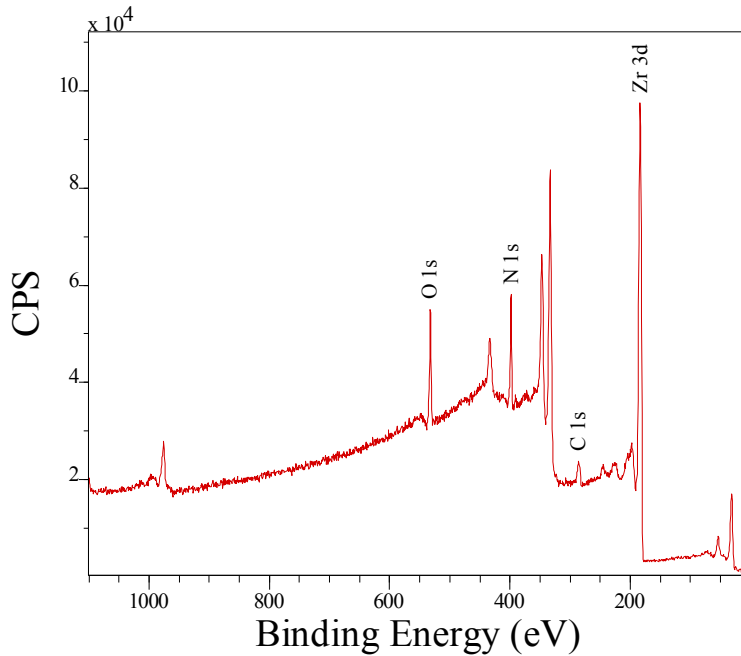


**Figure 4-3:** XPS data of  $ZrN_x$ /GaN interpreted through CasaXPS. The elemental composition is indicated by the samples' relative counts per second (CPS).

Element	Intensity/Area	RSF <sup>a</sup>	% Concentration
Zr 3d	85430.7	2.576	27.20
N 1s	22103.2	0.477	37.08
C 1s	4447.1	0.278	12.96
O 1s	22563.0	0.78	22.76

<sup>a</sup>See Ref. [50]

**Table 4-3:** Elemental composition of  $ZrN_x$ , determined from the peaks shown in Fig. 4-2. RSF refers to the relative sensitivity factor of each individual element, which is used to scale the measured peak areas.

### 4.3 C-V and 2DEG analysis

The 2DEG concentration observed for  $ZrN_x$  on N+ GaN is significantly higher than for N- GaN (Fig. 4-2), with the peak capacitance for the latter being approximately 100 times lower. This can be attributed to the change in Fermi level relative to the conduction band due to doping. As described in Section 4.1, N- GaN has a lower Fermi level than N+ GaN, which leads to a lower 2DEG concentration accumulating in the triangular quantum well.

The 2DEG concentrations for 4-7 nm of  $ZrN_x$  on N+ GaN are similar within error (Fig. 4-4). Although 5 nm of  $ZrN_x$  seems to produce slightly higher 2DEG, this is more likely due to the sample having a lower interface trap density (Table 4-4) as a result of variations in deposition quality among the samples. One likely source of interface traps is the presence of  $ZrO_2$  formed as a result of the oxidation described in Section 4.2. This is particularly evident for 1 nm of  $ZrN_x$ , which has a much lower 2DEG that suggests a higher density of interface traps present. Since it is much thinner than 4-7 nm of  $ZrN_x$ , a greater concentration of surface traps would accumulate in the layer due to oxide trapping.

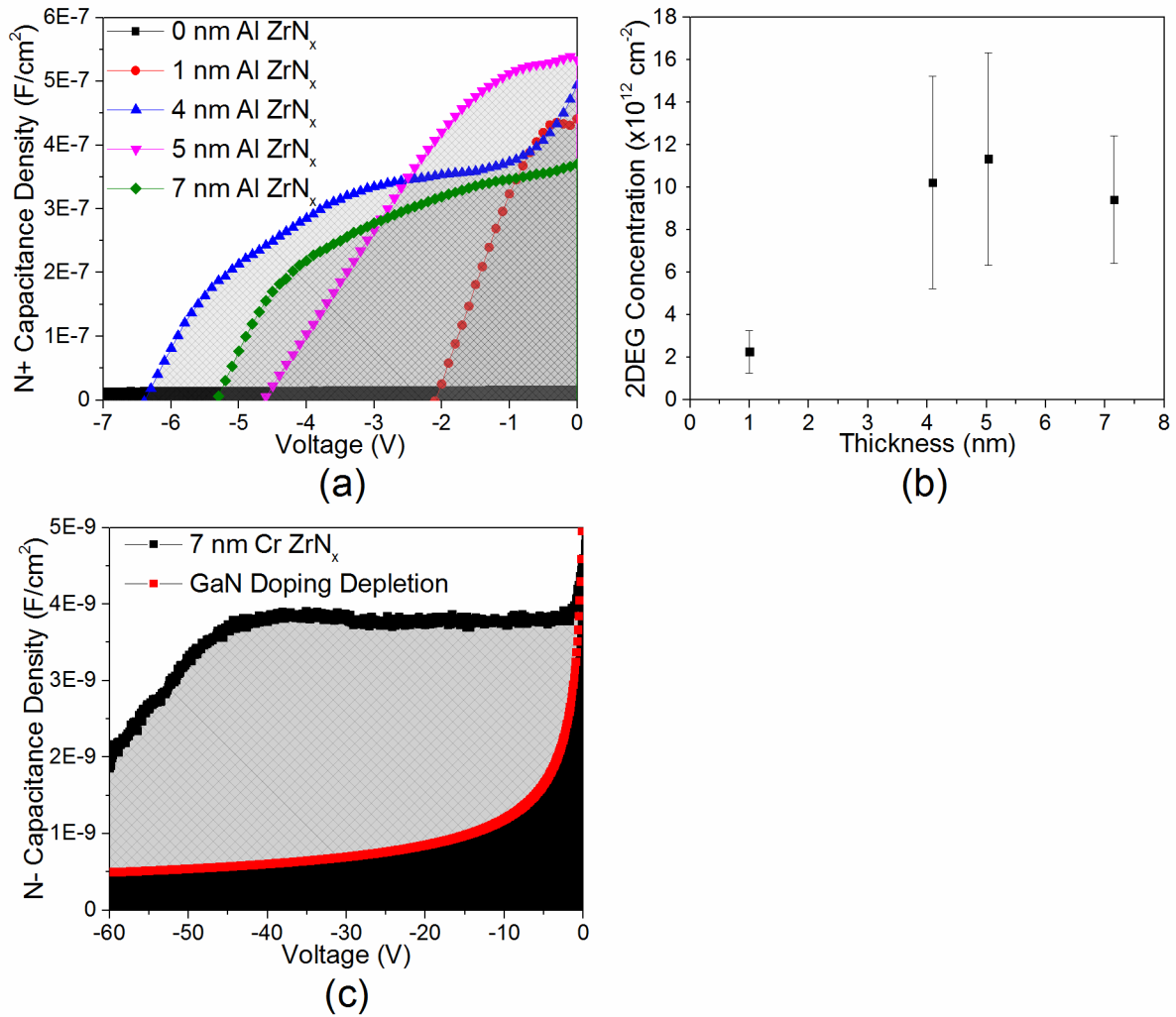


**Figure 4-4:** C-V plot of the 2DEG concentration for 1-7 nm of ZrN on (a) N+ GaN, with the 2DEG concentration shown in (b), and (c) N- GaN. The 0 nm Al case represents metal directly contacted to N+ GaN, while N- GaN is compared against the calculated depletion capacitance.

Doping (Metal)	Thickness (nm)	$Q_n$ ( $\times 10^{12}$ cm $^{-2}$ )	$D_{it}$ ( $\times 10^{12}$ eV $^{-1}$ cm $^{-2}$ )
N+ (Al)	1	2 $\pm$ 1	36
	4	10 $\pm$ 5	17
	5	11 $\pm$ 5	13
	7	9 $\pm$ 3	16
	0 (bare GaN)	1.4	N/A
N- (Cr)	7	1.0 $\pm$ 0.3	N/A
	0 (simulated)	0.3	N/A

**Table 4-4:** Comparison of 2DEG and interface trap concentrations with varying ZrN thickness, representing the difference between the total integrated charge and the bare GaN charge.

Overall, 2DEG concentrations of around  $1 \times 10^{13}$  cm $^{-2}$  have been achieved with 4-7 nm of ZrN $_x$  on N+ GaN, indicating that polarization effects are prominent between the two materials when ZrN $_x$  is in semiconducting phase. However, the 2DEG does not change significantly with ZrN $_x$  thickness, which indicates that barrier thickness has minimal effect on band bending. While the latter prediction is confirmed by the simulated band diagrams in Fig. 4-2, they also predicted minimal 2DEG due to their small quantum well depth. As the measured results indicate, polarization is stronger than the band diagrams indicate, and thus further simulations will need to be conducted in order to properly determine the band structure of ZrN $_x$ /GaN.

#### 4.4 I-V and contact analysis

Previous studies involving ZrN/GaN contacts have achieved ohmic behaviour, but with high resistance [21]. The high resistance was attributed to oxide formation and a high concentration of penetration pits on the ZrN/GaN surface. The study used reactive sputtering to deposit ZrN with a 180 nm thickness, so surface morphology may differ with ultrathin ZrN $_x$  deposited on GaN using ALD.

Fig. 4-5a shows a comparison of I-V curves for different contact metals on  $ZrN_x/GaN$ . The Cr contacts results in a rectifying characteristic compared to Al, which displays greater linearity. This hints that Al has a work function more closely matched to the  $ZrN_x$  electron affinity and that Cr creates a Schottky barrier with  $ZrN_x$ , just as predicted in Section 4.1. This leads to improved linearity when using Al, and shows that it is better suited to producing ohmic contacts than Cr.

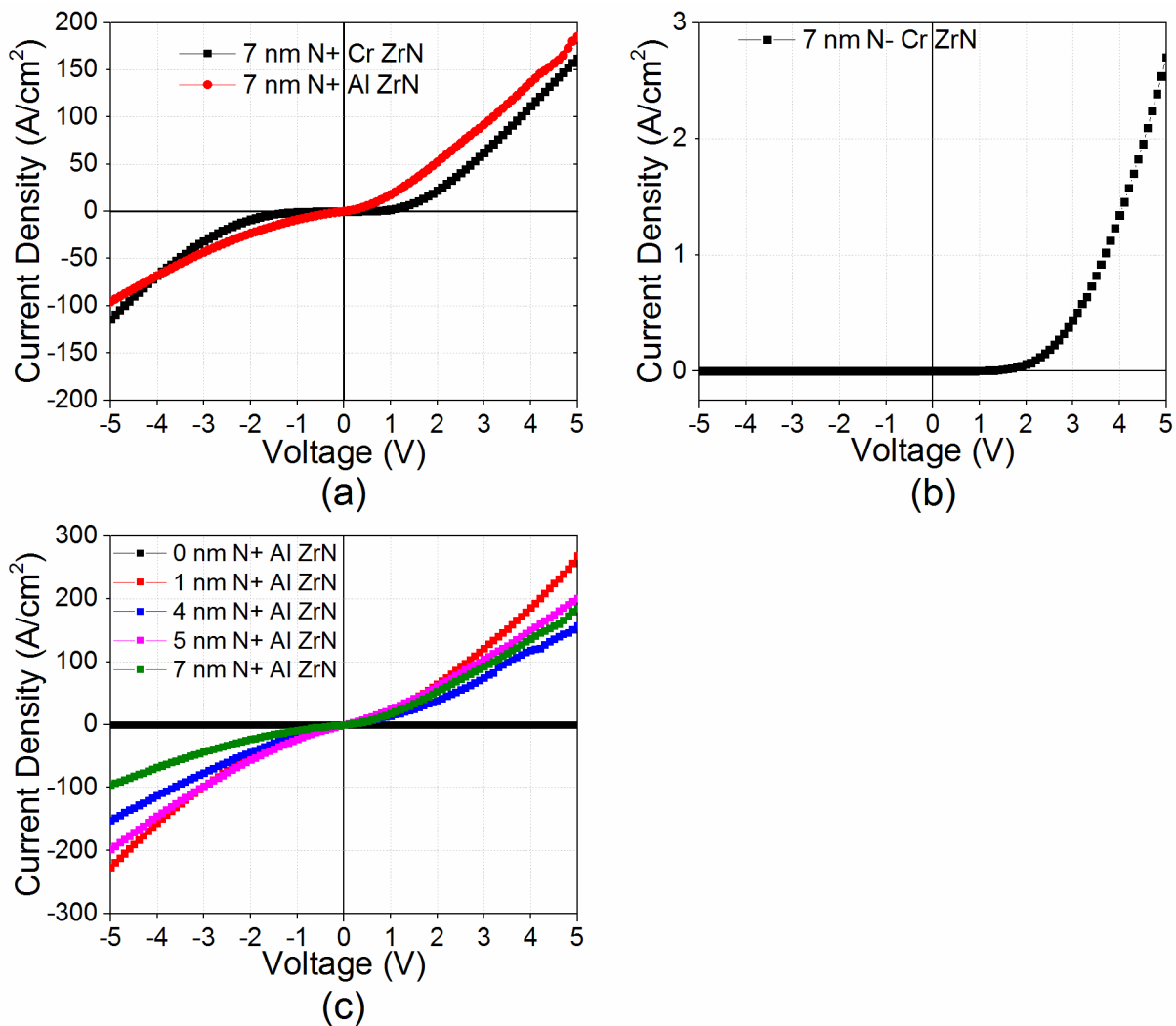


**Figure 4-5:** I-V plots of the  $ZrN_x/GaN$  heterojunction. Different contact metals are compared in (a), (b) shows N- GaN, and (c) compares varying  $ZrN_x$  thickness on N+ GaN.

Fig. 4-5b shows the I-V plot for  $ZrN_x$  on N- GaN, which, in contrast to N+ GaN, shows a rectifying junction with low current output. This is a result of the significantly reduced 2DEG concentration produced with N- GaN, and as previously mentioned in Section 4.3, suggests that the lowered Fermi level, which resulted from the reduced GaN doping, decreases the relative quantum well depth. Thus, obtaining ohmic contacts on N- GaN would be more challenging due to its less ideally matched band structure with  $ZrN_x$ .

With Al metal, the  $ZrN_x/N+$  GaN I-V curves (Fig. 4-5c) show a pseudo-ohmic relation within the 1-7 nm thickness range, with minimal change in resistance with varying  $ZrN_x$  thickness. In Section 3.5, it was theorized that the conductance for AlN on N+ GaN was primarily a function of 2DEG when deposited using low-temperature ALD. Section 4.3 previously established that the 2DEG concentration changes negligibly between 4-7 nm of  $ZrN_x$ , and this is reflected in the similar I-V curves shown in Fig. 4-4. The exception is 1 nm, which has a slightly higher conductance despite its lower 2DEG. Thus, the transmission coefficient at 1 nm would be high enough to offset the low 2DEG.

Although ohmic contacts have been demonstrated using  $ZrN_x/N+$  GaN, the conductance is low compared to the AlN/GaN samples (Fig. 3-9), likely due to oxide formation and surface defects reducing the conductance from its maximum potential. Thus, annealing studies were performed on the samples with the goal of attaining lower contact resistance from the  $ZrN_x/GaN$  heterojunction.

#### **4.5 Effect of annealing on contact resistance**

TLM characterization of 1 nm of  $ZrN_x$  on N+ GaN indicates a contact resistance of 27  $\Omega \cdot \text{mm}$ , or a specific contact resistance of  $0.027 \Omega \cdot \text{cm}^2$ . This is approximately 100 times higher

than AlN/GaN, which compromises its performance as MOSFET source/drain contacts. In order to reduce the contact resistance, a previous study [18] applied high-temperature (900°C – 1100°C) annealing to ZrN/Zr/GaN for 1 minute. Following this example, the ZrN<sub>x</sub>/GaN samples were annealed at temperatures from 700-1000°C in 100°C intervals for 1 minute. A comparison of the TLM I-V plots for the annealed samples, each consisting of 4 nm of ZrN<sub>x</sub> on N+ GaN, are

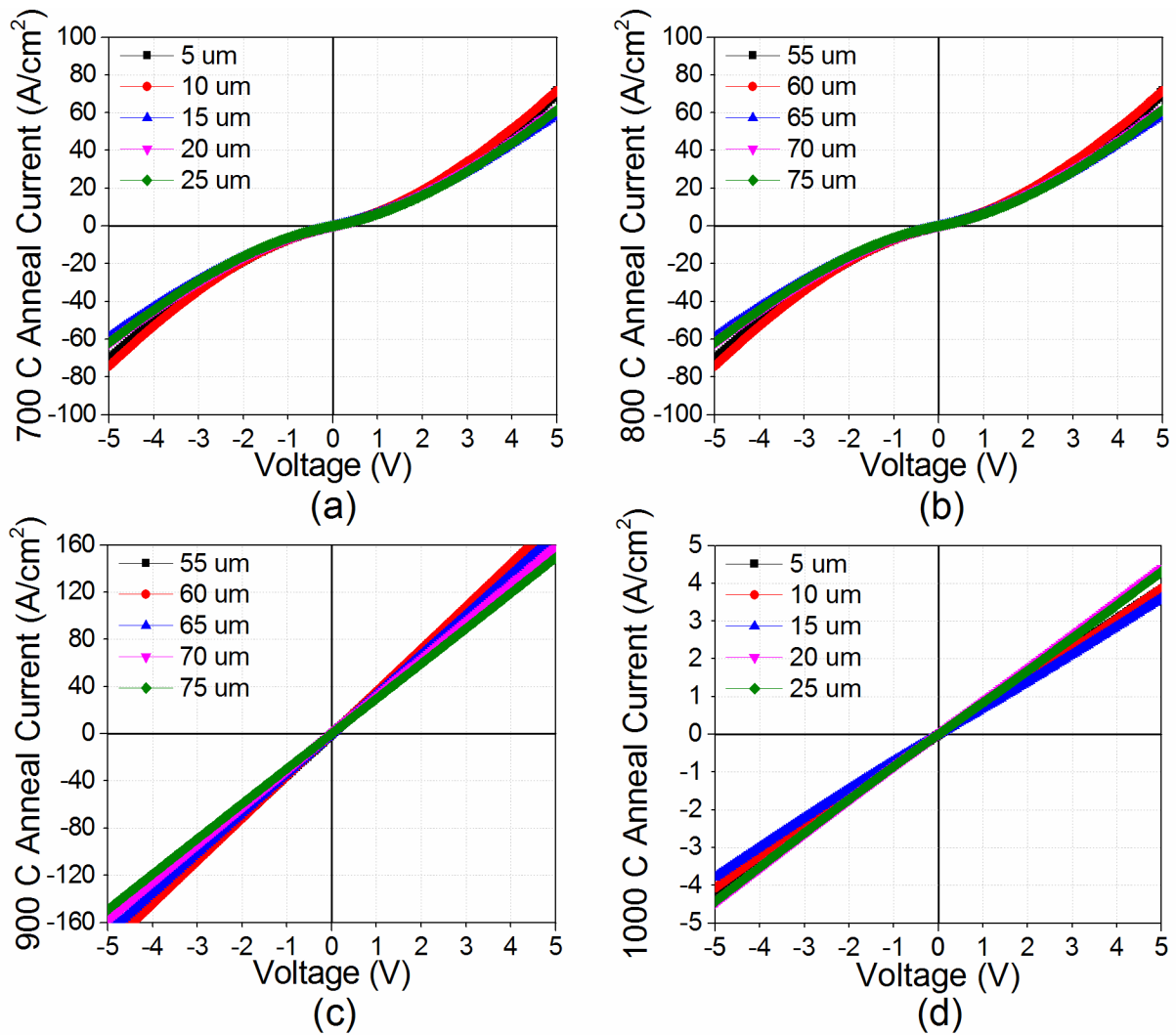


**Figure 4-6:** TLM I-V plots for 4 nm of ZrN<sub>x</sub> on N+ GaN, annealed at (a) 700°C, (b) 800°C, (c) 900°C, and (d) 1000°C. The equipment used to measure the I-V curves has an upper current limit of 0.1 A, which is reached in (c).

Thin Film	Metal	Thickness (nm)	Anneal Temperature (°C)	R <sub>c</sub>		R <sub>s</sub>
				(Ω·mm)	(Ω·cm <sup>2</sup> )	(Ω/sq)
AlN	Cr/Au	3.2	25	0.60	3.0E-04	355
	Al/Au			0.45	2.2E-04	341
ZrN <sub>x</sub>	Al/Au	1	25	28.0	2.8E-02	7930
			800	5.00	5.0E-03	543
			900	6.85	6.8E-03	612
			1000	12.7	1.3E-02	259
	4	700	23.4	2.3E-02	2970	
		800	22.4	2.2E-02	676	
		900	2.19	2.2E-03	390	
		1000	550	5.5E-01	14000	

**Table 4-5:** Comparison of TLM-derived resistances at varying annealing temperatures.

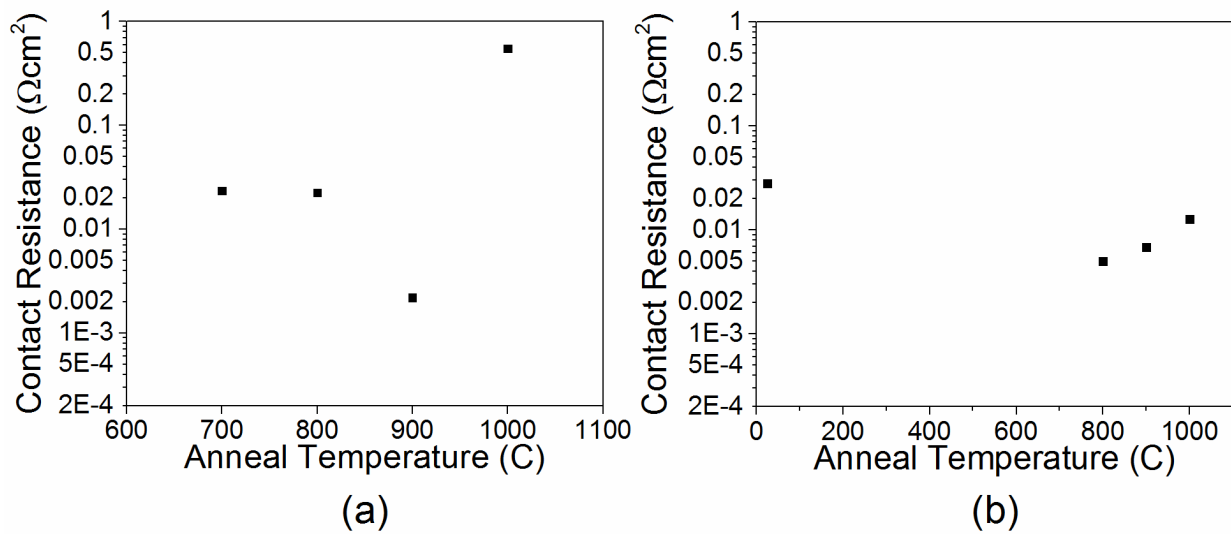


**Figure 4-7:** Comparison of contact resistance with annealing temperature for (a) 1 nm of ZrN<sub>x</sub> on N<sup>+</sup> GaN, and (b) 4 nm of ZrN<sub>x</sub> on N<sup>+</sup> GaN.

shown in Fig. 4-6. The contact resistance shows minimal change up to 800°C, as Table 4-5 and Fig. 4-7 indicate. Starting at 900°C, the resistance drops by a factor of 10 to  $2 \times 10^{-3} \Omega \cdot \text{cm}^2$  and the I-V plots become highly linear (Fig. 4-6c). Although further resistance drops are expected for higher temperatures [18], the contact resistance significantly rises at 1000°C. This is likely due to oxidation and pit formation on the ZrN<sub>x</sub> interface [51], and indicates that 900°C is the critical

annealing temperature before contact resistance degradation occurs. This critical temperature changes with  $ZrN_x$  thickness. With 1 nm of  $ZrN_x$ , the sample becomes ohmic at a lower 800°C temperature, albeit with a higher resistance of  $5 \times 10^{-3} \Omega \cdot cm^2$  (Fig. 4-7b). Higher annealing temperatures result in greater resistance as demonstrated by 4 nm, although the change is not as drastic. The lower critical annealing temperature is likely due to the thinner layer being more vulnerable to defects and oxidation. Although 1 nm of  $ZrN_x$  can achieve ohmic contacts at lower annealing temperatures, 4 nm of  $ZrN_x$  has greater potential for achieving low contact resistance.

The lowest contact resistance in  $ZrN_x/GaN$  is almost 10 times as high as un-annealed  $AlN/GaN$ , but with a comparable 390  $\Omega/sq$  sheet resistance. The material's improved breakdown reliability compensates for the higher resistance in the high electric field conditions of the GaN MOSFET gate/drain region, and future experiments intend to improve the contact resistance even further. In summary, 4 nm of  $ZrN_x$ , annealed at 900°C, has successfully demonstrated an ohmic contact with  $N^+$  GaN, thus serving as a suitable polarization layer replacement for  $AlN$  under high field conditions.

## 5 Conclusions

### 5.1 Process summary

In this thesis, quantum tunneling contacts were investigated for use in a GaN MOSFET. To this end, ultrathin AlN and ZrN<sub>x</sub> were deposited through PEALD on GaN samples with two varying doping concentrations. Their performance was analyzed through both simulation and electrical characterization. A self-consistent Schrödinger-Poisson solver was used to obtain the theoretical AlN/GaN and ZrN<sub>x</sub>/GaN band diagrams, from which the 2DEG concentration and electron transmission probability could be predicted. These were compared against results obtained from MOSCAP structures, which analyzed 2DEG charge through C-V profiling, and I-V curves measured from MOSCAP and TLM structures to analyze ohmic quality and contact resistance.

Chapter 2 outlined the ALD process, including material characterization through XRD and ellipsometry methods. The following sections explained device fabrication, C-V profiling, and I-V profiling methods.

Chapters 3 and 4 showed simulation and experimental results for contacts with deposited AlN and ZrN<sub>x</sub> layers respectively. The 2DEG concentration was analyzed with regards to layer thickness, polarization and interface traps. Contact quality was analyzed through comparing I-V linearity, contact resistance, and sheet resistance against the band diagram predicted transmission coefficients. The effects of annealing temperature on AlN and ZrN<sub>x</sub> resistance were also analyzed.

## 5.2 Key observations

2DEG concentrations of around  $2 \times 10^{13} \text{ cm}^{-2}$  or higher were achieved with AlN on both N<sup>+</sup> and N<sup>-</sup> GaN. These peak concentrations were observed at differing AlN thicknesses depending on doping, with a lower strain relaxation critical thickness of 4.5 nm observed on N<sup>+</sup> GaN, while peak 2DEG occurs at 5.7 nm for N<sup>-</sup> GaN. In addition, while strain relaxation occurs at thicknesses higher than critical for N<sup>+</sup> GaN as expected, N<sup>-</sup> GaN demonstrates low 2DEG concentration relative to a simulated fully strained heterojunction at lower thicknesses. The high degree of relaxation observed on N<sup>-</sup> GaN, which has been attributed to interface trap influence, suggests a greater degree of polarization when AlN is deposited on higher-doped GaN using low-temperature ALD. Thus, the higher dopant density may encourage single-crystal growth.

For the ZrN<sub>x</sub>/GaN heterojunction, 2DEG concentrations of  $1 \times 10^{13} \text{ cm}^{-2}$  were achieved on N<sup>+</sup> GaN, which demonstrates the influence of polarization between the two materials and suggests that semiconducting ZrN<sub>x</sub> is a viable material to achieve 2DEG with GaN. Despite the high variation of 2DEG concentration with AlN/GaN, ZrN<sub>x</sub>/GaN shows little change in 2DEG with thickness, and any discrepancies were attributed to defect-induced interface traps arising from processing inconsistencies. This lack of variation reflects a low band offset between the two materials. Since the conduction bands are closely matched, thickness would have a minimal impact on band bending. Further evidence of a low band offset is that the 2DEG concentration becomes much lower with N<sup>-</sup> GaN compared to N<sup>+</sup> GaN, which is the result of the Fermi level rising relative to the conduction band for higher GaN doping. This is not observed in AlN/GaN since the band offset is much higher than the change in Fermi level with doping.

In accordance with the varying 2DEG concentrations, the AlN/GaN samples demonstrated significant I-V variation with doping and thickness. I-V conductance and linearity with N+ GaN was more dependent on 2DEG concentration. In contrast, N- GaN was more influenced by barrier thickness and the predicted transmission coefficient from simulation. Temperature-variant measurements have shown that tunneling does not account for all current produced in ohmic contacts. Ultimately, 3.2 nm of AlN on N+ GaN demonstrated a low  $2 \times 10^{-4} \Omega \cdot \text{cm}^{-2}$  contact resistance, showing that low-resistance ohmic contacts on GaN can be achieved using an entirely low-temperature process.

For  $\text{ZrN}_x/\text{GaN}$  samples, ohmic contacts were achieved on N+ GaN with Al contacts, while showing non-ohmic characteristics with either N- GaN or Cr contacts. Although the contact resistance was initially measured as  $2 \times 10^{-2} \Omega \cdot \text{cm}^{-2}$ , post-deposition annealing dropped the resistance to a minimum  $2 \times 10^{-3} \Omega \cdot \text{cm}^{-2}$  with 4 nm of  $\text{ZrN}_x$  at  $900^\circ\text{C}$ . This varied with  $\text{ZrN}_x$  thickness, as 1 nm of  $\text{ZrN}_x$  achieved  $5 \times 10^{-3} \Omega \cdot \text{cm}^{-2}$  at  $800^\circ\text{C}$ , degrading at higher temperatures. Further experiments aim to lower the contact resistance further, but these results demonstrate that ohmic contacts on  $\text{ZrN}_x/\text{GaN}$  with some degree of polarization-induced charge are achievable, which makes it a potential alternative to AlN/GaN.

### **5.3 Future work**

The full GaN MOSFET structure is currently under investigation for design and characterization. Fig. 5-1 shows preliminary I-V characterization of the device. The structure demonstrates an ideal saturation onset voltage for GaN devices and enhancement-mode performance, with current scaling with gate voltage, which is a promising start. Issues currently facing the device include the low output current of AlN on N- GaN. In addition, the device

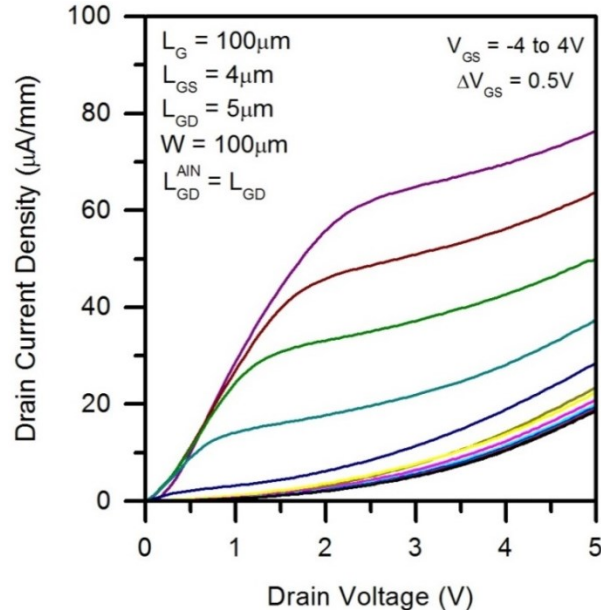


**Figure 5-1:** I-V family of curves for the GaN MOSFET based on 40 cycles of AlN on N- GaN.

produces significant leakage current as a result of the high electric field present at the drain-side gate edge [48]. Further annealing studies of AlN on N- GaN will be conducted with the intent of improving its conductance.  $ZrN_x$  will be integrated and tested into the drain contact region as a potential substitute for aluminum due to its higher breakdown field capacity.

We have successfully reached the  $<0.5 \Omega \cdot \text{mm}$  contact resistance target [43] for AlN on GaN with Al/Au contacts. However, Al is not a reliable metal for device contacts as its low melting point ( $660^\circ\text{C}$ ) [52] makes it unstable at high temperatures. Thus, Cr/Au contacts will be investigated further through post-deposition annealing experiments similar to those conducted with  $ZrN_x$ . Fig. 5-2 shows the I-V curves for 40 cycles of AlN on N- GaN annealed at  $400\text{--}900^\circ\text{C}$ . Optimal conductance and linearity, comparable to N+ GaN, are achieved at  $700^\circ\text{C}$  for an annealing time longer than the expected 30 s. From the initial data, low contact resistances are expected within the  $600^\circ\text{C} - 800^\circ\text{C}$  annealing window for 1 min or greater, which will be tested through TLM characterization in future studies. Achieving low contact resistance on N- GaN

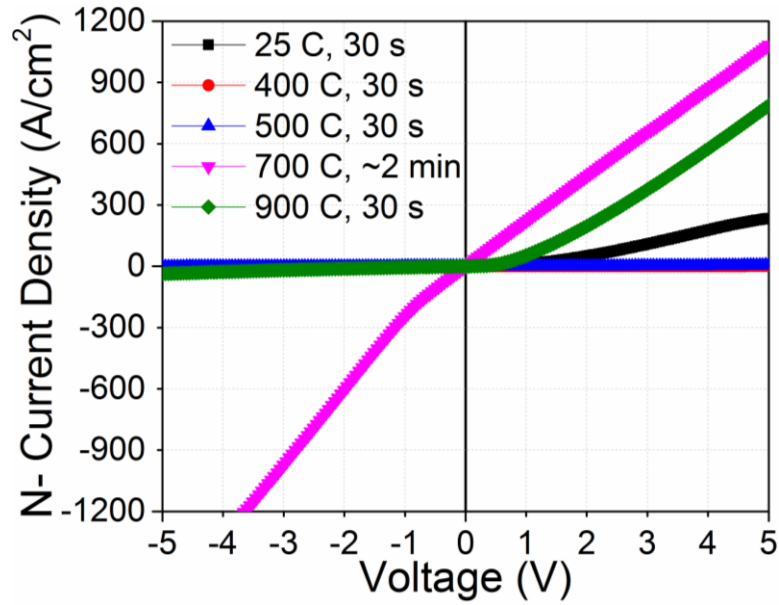


**Figure 5-2:** I-V comparison for different annealing temperatures for 40 cycles of AlN on N-GaN.

would be highly beneficial for the GaN MOSFET design by removing the need for N<sup>+</sup> ion implants, with the doping gradient achieved with n-dopant concentrations lower than N-GaN.

Although ohmic contacts have been successfully demonstrated on ZrN<sub>x</sub>/GaN, the contact resistance is still more than 4 times higher than the 0.5 Ω•mm target, which makes it inferior to AlN with respect to resistance. One possible improvement can be made in its stoichiometry. Our future ZrN<sub>x</sub> studies will involve investigating the change in its electrical properties with varying nitride concentration ranging from metallic ZrN to insulating Zr<sub>3</sub>N<sub>4</sub>. We intend to reduce the contact resistance to levels comparable to AlN/GaN by minimizing the nitrogen concentration in ZrN<sub>x</sub> to make it more metallic. In addition, further investigations in determining the energy band properties of ZrN<sub>x</sub>/GaN will be conducted, since contradictions currently exist between experiment and simulation.

## 5.4 Final remarks

This research has successfully demonstrated low-resistance ohmic quantum tunneling contacts with AlN and ZrN<sub>x</sub> thin films deposited on GaN using low-temperature PEALD. This deposition process has allowed a high degree of control over the polarization of AlN/GaN, with which high 2DEG concentrations and low contact resistances can be attained. ZrN<sub>x</sub> looks to be a promising material for resolving the ongoing issue of drain breakdown in GaN power devices for its ability to withstand high fields, and further improvements can be made by investigating its unique stoichiometric properties.

Along with ZrO<sub>2</sub> being previously established as a suitable oxide material, these findings have presented the necessary tools for designing and developing a full GaN MOSFET. In addition, low-temperature PEALD is simple, inexpensive, and easily integrated into industrial processes, which will benefit mass production of the devices. By optimizing contact resistance and breakdown electric field, future research into PEALD thin films aims to further realize the immense potential of the GaN MOSFET for reliable and highly energy efficient power electronic switching devices.

## 6 References

- [1] T. P. Chow, "SiC and GaN bipolar power devices," *Solid-State Electronics*, Vol. 44, pp. 277-301, Feb. 2000
- [2] B. J. Baliga, "Power Semiconductor Device Figure of Merit for High-Frequency Applications," *IEEE Electron Device Letters*, Vol. 10, No. 10, pp. 455-457, Oct. 1989
- [3] M. Asif Khan, J. N. Kuznia, J. M. Van Hove, N. Pan, and J. Carter. "Observation of a twodimensional electron gas in low pressure metalorganic chemical vapor deposited GaN-Al<sub>x</sub>Ga<sub>1-x</sub>N heterojunctions," *Applied Physics Letters* Vol. 60, No. 24, pp. 3027-3029, Jun. 1992
- [4] T. Marron, "GaN Based FETs for Power Switching Applications"
- [5] K. Bothe, M. Johnson, D. Barlage, "TCAD Modeling and Simulation of a Field Plated GaN MOSFET for High Voltage Applications," *CS MANTECH Conference*, May 16th-19th, 2011, Palm Springs, California, USA
- [6] K.S. Boutros et al., "Normally-off 5A/1100V GaN-on-silicon device for high voltage applications," *IEDM IEEE International*, pp. 161-163, Dec. 2013
- [7] J.S. Jur et al., "Epitaxial rare earth oxide growth on GaN for enhancement-mode MOSFETs," *CS MANTECH Conference*, April 14-17, 2008, Chicago, Illinois, USA
- [8] K. M. Bothe et al, "Electrical comparison of HfO<sub>2</sub> and ZrO<sub>2</sub> gate dielectrics on GaN," *IEEE Transactions on Electron Devices*, Vol. 60, No. 12, pp. 4119-4124, Dec. 2013
- [9] J. P. Ibbetson et al., "Polarization effects, surface states, and the source of electrons in AlGa<sub>N</sub>/Ga<sub>N</sub> heterostructure field effect transistors," *Applied Physics Letters*, Vol. 77, No. 2, pp. 250-252, Jul. 2000
- [10] O. Ambacher et al., "Two dimensional electron gases induced by spontaneous and piezoelectric polarization in undoped and doped AlGa<sub>N</sub>-Ga<sub>N</sub> heterostructures," *Journal of Applied Physics*, Vol. 87, No. 1, pp. 334-344, Jan. 2000

- [11] F. Bernardini, V. Fiorentini, and D. Vanderbilt, "Spontaneous polarization and piezoelectric constants of III-V nitrides," *Physical Review B*, Vol. 56, No. 16, pp. R10 24-27, Oct. 1997
- [12] J. W. Matthews and A. E. Blakeslee, "Defects in epitaxial multilayers," *Journal of Crystal Growth*, Vol. 27, pp. 118-125, Dec. 1974
- [13] A. Fischer, H. Richter, and H. Kuhne, "New Approach in Equilibrium Theory for Strained Layer Relaxation," *Physical Review Letters*, Vol. 73, No. 20, pp. 2712-2715, Nov. 1994
- [14] I. P. Smorchkova et al., "AlN/GaN and (Al,Ga)N/AlN/GaN two-dimensional electron gas structures grown by plasma-assisted molecular-beam epitaxy," *Journal of Applied Physics*, Vol. 90, No. 10, pp. 5196-5201, Nov. 2001.
- [15] Y. Cao and D. Jena, "High-mobility window for two-dimensional electron gases at ultrathin AlN/GaN heterojunctions," *Applied Physics Letters* Vol. 90, 182112, May 2007
- [16] A. Adikimenakis et al., "High electron mobility transistors based on the AlN/GaN heterojunction," *Microelectronic Engineering*, Vol. 86, pp. 1071-1073 (2009).
- [17] W. Y. Ching, Y. N. Xu, and L. Ouyang, "Electronic and dielectric properties of insulating  $Zr_3N_4$ ," *Physical Review B*, Vol. 66, 235106 (2002)
- [18] S. D. Wolter, B. P. Luther, S. E. Mohny, R. F. Karlicek, and R. S. Kernc, "Thermally Stable ZrN/Zr/n-GaN Ohmic Contacts," *Electrochemical and Solid-State Letters*, Vol. 2, No. 3, pp. 151-153, Jan. 1999
- [19] Z. An, C. Men, Z. Xu, P. K. Chu, and C. Lin, "Electrical properties of AlN thin films prepared by ion beam enhanced deposition," *Surface and Coatings Technology*, Vol. 196, pp. 130-134, Jun. 2005
- [20] M. A. Signore, D. Valerini, L. Tapfer, G. Caretto, and A. Rizzo, "Zirconium nitride films deposited in (Ar+N<sub>2</sub>+H<sub>2</sub>) sputtering atmosphere: Optical, structural, and electrical properties," *Journal of Vacuum Science and Technology A*, Vol. 29, No. 6, 061507, Nov/Dec 2011

- [21] H. B. Bhuvaneshwari, K. P. S. S. Hembram, V. R. Reddy, and G. M. Rao, "Studies on metal–semiconductor contacts with ZrN as metal layer," *Optoelectronics and Advanced Materials*, Vol. 1, No. 6, pp. 294 – 298, June 2007
- [22] A. Foroughi-Abari and K. C. Cadien, "In Situ Spectroscopic Ellipsometry Study of Plasma-Enhanced ALD of Al<sub>2</sub>O<sub>3</sub> on Chromium Substrates," *Journal of the Electrochemical Society*, Vol. 159, pp. D59-64, Dec. 2011
- [23] S. E. Potts et al., "Low Temperature Plasma-Enhanced Atomic Layer Deposition of Metal Oxide Thin Films," *Journal of the Electrochemical Society*, Vol. 157, No. 7, pp. P66-74, May 2011
- [24] S. A. Smith, C. A. Wolden, M. D. Bremser, A. D. Hanser, R. F. Davis, and W. V. Lampert, "High rate and selective etching of GaN, AlGa<sub>N</sub>, and AlN using an inductively coupled plasma," *Applied Physics Letters*, Vol. 71, No. 25, pp. 3631-3633, Dec. 1997
- [25] P. A. Tipler and R. A. Llewellyn, "Modern Physics," 3rd Ed., W.H. Freeman, 1999
- [26] K. Bothe, M. Johnson, and D. Barlage, "TCAD modeling and simulation of a field plated GaN MOSFET for high voltage applications," *CS MANTECH Conference*, May 16th-19th, 2011, Palm Springs, California, USA
- [27] K. Voon, K. Bothe, P. Motamedi, K. Cadien, D. Barlage "Engineered tunneling contacts with atomic layer deposition of AlN on GaN," *CS MANTECH Conference*, May 19-22th, 2014, Denver, Colorado, USA
- [28] H. Kroemer, W. Y. Chien, J. S. Harris Jr., and D. D. Edwall, "Measurement of isotope heterojunction barriers by C-V profiling," *Applied Physics Letters*, Vol. 36, No. 4, pp. 295-297, Feb. 1980
- [29] M. Miczek, C. Mizue, T. Hashizume, and B. Adamowicz, "Effects of interface states and temperature on the C-V behavior of metal/insulator/AlGa<sub>N</sub>/Ga<sub>N</sub> heterostructure capacitors," *Journal of Applied Physics*, Vol. 103, 104510, May 2008
- [30] L. M. Terman, "An investigation of surface states at a silicon/silicon oxide interface employing metal-oxide-silicon," *Solid-State Electronics* Vol. 5, pp. 285-299, Feb. 1962

- [31] D. K. Schroder, "Semiconductor Material and Device Characterization" (Wiley-IEEE Press, 2006).
- [32] S. M. Sze and K. K. Ng, "Physics of Semiconductor Devices" (Wiley-Interscience, 2006).
- [33] K. Voon, K. Bothe, P. Motamedi, K. Cadien, D. Barlage "Polarization charge properties of low-temperature atomic layer deposition of AlN on GaN," *Journal of Physics D: Applied Physics*, Vol. 47, No. 34, 345104, Aug. 2014
- [34] M. Alevli, C. Ozgit, I. Donmez, and N. Biyikli, "Structural properties of AlN films deposited by plasma-enhanced atomic layer deposition at different growth temperatures," *Physica Status Solidi (a)*, Vol. 209, No. 2, 266–271 (2012)
- [35] C. A. Hurni, H. Kroemer, U. K. Mishra, and J. S. Speck "Capacitance-voltage profiling on polar III-nitride heterostructures," *Journal of Applied Physics*, Vol. 112, 083704, Oct. 2012
- [36] G. Koley and M. G. Spencer, "Surface potential measurements on GaN and AlGaIn/GaN heterostructures by scanning Kelvin probe microscopy," *Journal of Applied Physics*, Vol. 90, No. 1, pp. 337-344, Jul. 2001
- [37] J. Osvald, "Interface traps in insulator/AlGaIn/GaN heterostructure capacitors," *ASDAM 2012*, The Ninth International Conference on Advanced Semiconductor Devices and Microsystems, pp. 59-62, November 11–15, 2012, Smolenice, Slovakia
- [38] M. Suzuki, T. Uenoyama, and A. Yanase, "First-principles calculations of effective-mass parameters of AlN and GaN," *Physical Review B*, Vol. 52, No. 11, pp. 8132-8139, Sept. 1995
- [39] C. I. Wu and A. Kahn, "Electronic states at aluminum nitride (0001)-1x1 surfaces," *Applied Physics Letters*, Vol. 74, No. 4, pp. 546-548, Jan. 1999
- [40] V. Bougrov, M. E. Levinshtein, S. L. Rumyantsev, and A. Zubrilov, "Properties of Advanced Semiconductor Materials GaN, AlN, InN, BN, SiC, SiGe," John Wiley & Sons, Inc., New York, 2001, 1-30

- [41] I.H. Tan, G.L. Snider, L.D. Chang, and E.L. Hu, "A selfconsistent solution of Schrodinger-Poisson equations using a nonuniform mesh," *Journal of Applied Physics*, Vol. 68, No. 8, pp. 4071-4076, Oct. 1990
- [42] Y. C. Lee, T. T. Kao, J. J. Merola, C. Lian, D. Wang, D. Hou, and S. C. Shen, "Observation on Slow Carrier Trapping in AlGaIn/GaN Schottky Barrier Diodes and MIS Capacitors," *CS MANTECH Conference*, May 19-22th, 2014, Denver, Colorado, USA
- [43] H. Yang, Y. Son, S. Choi, and H. Hwang, "Improved conductance method for determining interface trap density of metal-oxide semiconductor device with high series resistance," *Japanese Journal of Applied Physics*, Vol. 44, No. 48, pp. L 1460-L 1462, Nov. 2005
- [44] H. Tsuji, Y. Kamakura, and K. Taniguchi, "Simple extraction method of interface trap density in thin-film transistors," *J. Electrochem. Soc.*, Vol. 156, No. 6, pp. H430-H433, Apr. 2009
- [45] Y. Ando and T. Itoh, "Calculation of transmission tunneling current across arbitrary potential barriers," *Applied Physics Letters*, Vol. 61, No. 4, pp. 1497-1502, Feb. 1987
- [46] T. Zimmermann et al., "Formation of ohmic contacts to ultra-thin channel AlN/GaN HEMTs," *Physica Status Solidi (c)*, Vol. 5, No. 6, pp. 2030-2032, Apr. 2008
- [47] K. Chabak et al. "Processing Methods for Low Ohmic Contact Resistance in AlN/GaN MOSHEMTs," *CS MANTECH Conference*, May 18-21th, 2009, Tampa, Florida, USA
- [48] J. Si, J. Wei, W. Chen, and B. Zhang, "Electric field distribution around drain-side gate edge in AlGaIn/GaN HEMTs: analytical approach," *IEEE Transactions on Electron Devices*, Vol. 60, No. 10, pp. 3223-3229, Oct. 2013
- [49] Y. Gotoh, H. Tsuji, and J. Ishikawa, "Measurement of work function of transition metal nitride and carbide thin films," *Journal of Vacuum Science & Technology B*, Vol. 21, No. 4, pp. 1607-1611, Jul. 2003
- [50] J. F. Moulder and J. Chastain, "Handbook of X-ray Photoelectron Spectroscopy" (Physical Electronics Division, Perkin-Elmer Corporation, 1992)

[51] H. B. Bhuvaneswari, V. R. Reddy, R. Chandramani, and G. M. Rao, "Annealing effects on zirconium nitride films," *Applied Surface Science*, Vol. 230, No. 6, pp. 88-93, Apr. 2004

[52] M. L. Lee, J. K. Sheu, and C. C. Hu, "Nonalloyed Cr/Au-based Ohmic contacts to n-GaN," *Applied Physics Letters*, Vol. 91, No. 18, 182106, Oct. 2007